Acta Pharmaceutica Sinica B 2025;15(5):2655−2672

Chinese Pharmaceutical Association
Institute of Materia Medica, Chinese Academy of Medical Sciences

Acta Pharmaceutica Sinica B

www.elsevier.com/locate/apsb
www.sciencedirect.com

ORIGINAL ARTICLE

Metabolic reprogramming nanomedicine potentiates colon cancer sonodynamic immunotherapy by inhibiting the CD39/CD73/ADO pathway

Yuanyuan Zhang[a,†], Weiwei Jin[b,†], Zhichao Deng[a], Bowen Gao[a], Yuanyuan Zhu[a], Junlong Fu[a], Chenxi Xu[a], Wenlong Wang[a], Ting Bai[c], Lianying Jiao[a], Hao Wu[a], Mingxin Zhang[d,*], Mingzhen Zhang[a,*]

[a]*School of Basic Medical Sciences, Xi'an Jiaotong University, Xi'an 710061, China*
[b]*General Surgery, Cancer Center, Department of Gastrointestinal and Pancreatic Surgery, Zhejiang Provincial People's Hospital (Affiliated People's Hospital), Hangzhou Medical College, Hangzhou 310014, China*
[c]*Department of Cardiovascular Medicine, the First Affiliated Hospital, Xi'an Jiaotong University, Xi'an 710077, China*
[d]*Department of Gastroenterology, the First Affiliated Hospital of Xi'an Medical University, Xi'an 710077, China*

Received 7 November 2024; received in revised form 1 March 2025; accepted 14 March 2025

KEY WORDS

Sonodynamic therapy;
Immunotherapy;
Ag_2S quantum dots;
POM1;
Colon cancer;
CD39/CD73/ADO pathway;
Immunogenic cell death;
Anti-tumor immunity

Abstract Sonodynamic therapy (SDT) can potentially induce immunogenic cell death in tumor cells, leading to the release of ATP, and facilitating the initiation of an immune response. Nevertheless, the enzymes CD39 and CD73 can swiftly convert ATP into immunosuppressive adenosine (ADO), resulting in an immunosuppressive tumor microenvironment (TME). This study introduced a nanomedicine (QD/POM1@NP@M) engineered to reprogram TME by modulating the CD39/CD73/ADO pathway. The nanomedicine encapsulated sonosensitizers silver sulfide quantum dots, and the CD39 inhibitor POM1, while also incorporating homologous tumor cell membranes to enhance targeting capabilities. This integrated approach, on the one hand, stimulates the release of ATP *via* SDT, thereby initiating the immune response. In addition, it reduced the accumulation of ADO by inhibiting CD39 activity, which ameliorated the immunosuppressive TME. Upon administration, the nanomedicine demonstrated

*Corresponding authors.
E-mail addresses: zmx3115@xiyi.edu.cn (Mingxin Zhang), mzhang21@xjtu.edu.cn (Mingzhen Zhang).
†These authors made equal contributions to this work.
Peer review under the responsibility of Chinese Pharmaceutical Association and Institute of Materia Medica, Chinese Academy of Medical Sciences.

https://doi.org/10.1016/j.apsb.2025.03.046

substantial anti-tumor efficacy by facilitating the infiltration of anti-tumor immune cells, while reducing the immunosuppressive cells. This modulation effectively transformed the TME from an immunologically "cold" state to a "hot" state. Furthermore, combined with the checkpoint inhibitor α-PDL1, the nanomedicine augmented systemic anti-tumor immunity and promoted the establishment of long-term immune memory. This study provides an innovative strategy for combining non-invasive SDT and ATP-driven immunotherapy, offering new ideas for future cancer treatment.

1. Introduction

Numerous non-invasive therapies, including radiation therapy and photothermal therapy, have the potential to elicit tumor immunity through the induction of immunogenic cell death (ICD) in tumor cells[1,2]. Sonodynamic therapy (SDT) is especially preferred due to its capability for deep tissue penetration and high precision[3]. However, conventional organic sonosensitizers, such as hematoporphyrins and photopigments, are characterized by low molecular bioavailability, unstable chemical, biological properties, and high phototoxicity, which collectively result in suboptimal therapeutic efficacy in SDT[4]. In recent years, innovative sonosensitizer nanoparticles exhibiting stable properties and reduced phototoxicity have been developed, showing promising acoustochemical characteristics that address the limitations of traditional organic sensitizers. Notably, silver sulfide quantum dots (Ag_2S QDs) have been reported to possess outstanding sonosensitizer properties, along with excellent biocompatibility, prolonged blood circulation, and imaging capabilities in the near-infrared II region[5,6]. These attributes position Ag_2S QDs as a valuable asset with significant advantages and potential for clinical application in SDT.

Ultrasound can accurately activate sonosensitizers at the target site, leading to the generation of substantial quantities of reactive oxygen species (ROS), which cause oxidative stress damage to cells and subsequently induce ICD[7,8]. Cells undergoing ICD can release damage-associated molecular patterns (DAMPs) such as calreticulin (CRT), high mobility group box 1 (HMGB1), adenosine triphosphate (ATP), tumor-associated antigens, and other immunogenic signals[9]. During this process, ATP functions as a "find me" signal that initiates T-cell immunity by promoting macrophage polarization and facilitating the infiltration and antigen presentation of dendritic cells (DCs)[10,11].

In the tumor microenvironment (TME), ATP is rapidly degraded into the immunosuppressive molecule adenosine (ADO) by the action of two ubiquitously expressed nucleic acid exonucleases, CD39 and CD73. This degradation process attenuates the immune activation effect of ICD. CD39, also known as ectonucleoside triphosphate diphosphohydrolase 1 (ENTPase 1), catalyzes the hydrolysis of ATP to adenosine 5′-monophosphate (5′-AMP)[12]. Subsequently, CD73, an exonuclease 5′-nucleotidase, further converts 5′-AMP into ADO[13]. ADO interacts with adenosine receptors, such as A2A and A2B, on immune cells, eliciting various immunosuppressive effects[14]. Specifically, ADO facilitates the accumulation of intracellular cyclic AMP in T cells, thereby inhibiting the proliferation of effector T lymphocytes and the secretion of inflammatory cytokines[15]. ADO can also promote the polarization of tumor-associated macrophages (TAMs) from an anti-tumorigenic M1-like phenotype to a tumor-promoting M2-like phenotype. Additionally, ADO serves as a critical effector molecule in regulatory T cells (Tregs), where it plays a role in suppressing anti-tumor immunity by enhancing Tregs activity[16]. Unfortunately, the ectonucleotidases CD39 and CD73 are frequently overexpressed in a variety of solid tumors[17]. Consequently, while SDT can induce ICD in tumor cells, the elevated expression of these ectonucleotidases often mitigates the immunogenicity of the dying tumor cells, thereby limiting the overall efficacy of tumor treatment and potentially leading to tumor recurrence[18].

Therefore, preserving or augmenting ATP concentrations within the TME is crucial for sustaining the anti-tumor immune response initiated by SDT. Presently, numerous inhibitors targeting the CD39/CD73/ADO pathway have been developed to revitalize the immune response by mitigating ADO accumulation[19]. Among these, CD39, the rate-limiting extracellular enzyme responsible for ATP degradation, plays a crucial role in maintaining the dynamic balance of extracellular ATP within the TME[20]. Currently, numerous drugs targeting CD39 have advanced to clinical trial phases[21]. The CD39 small molecule inhibitor, sodium polyxotungstate (POM-1), has been shown to not only alleviate ADO-driven immunosuppression but also stabilize ATP-mediated immune stimulation in the TME, thereby enhancing anti-tumor responses[22,23]. CD39 receptors are extensively distributed throughout the body. Consequently, the non-targeted administration of potent CD39 inhibitors can disrupt immune cell function and potentially induce immune-related adverse effects[24,25]. Advances in nano-delivery technologies have enabled targeted drug delivery and spatiotemporal controlled release of therapeutics[26]. Thus, the development of innovative nano-delivery strategies for the combination therapy of ICD inducers and CD39 inhibitors holds significant promise. This nano-delivery strategy can utilize ICD inducers to effectively eradicate tumor cells and minimize the off-target toxicity of immunosuppressants, thereby improving therapeutic safety.

To implement this combined therapeutic strategy, a biomimetic nanomedicine platform denoted as QD/POM1@NP@M was engineered. In this work, poly(lactic-*co*-glycolic acid) (PLGA) together with the cationic lipid 1,2-dioleoyl-3-trimethylammonium propane (DOTAP) formed the outer shell of the nanocarrier with a core wrapped with hydrophobic sonosensitizers Ag_2S QDs and hydrophilic CD39 inhibitor POM1. Subsequently, homologous tumor cell membranes were encapsulated on the surface of the PLGA-based nanocarrier for their mimicry. After tail vein injection, QD/POM1@NP@M efficiently accumulates at the tumor site by taking advantage of the intrinsic homing ability of homologous tumor cell membranes. Under ultrasound irradiation, Ag_2S QDs generated large amounts of ROS causing cell death leading to sustained release of ATP. Meanwhile, POM1 inhibits CD39-mediated ATP breakdown in immune cells, resulting in increased

ATP levels within the TME. Elevated ATP levels enhance DCs maturation and antigen presentation, ultimately activating T cell-mediated immune responses. In addition, reduced accumulation of immunosuppressive ADO promotes macrophage polarization toward the M1 phenotype and attenuates Tregs activity and its immunosuppression of T cells. Through comprehensive immune cell regulation and TME reprogramming, QD/POM1@NP@M facilitates the transition from a "cold" tumor to a "hot" tumor. When combined with the immune checkpoint inhibitor PD-L1, QD/POM1@NP@M exhibits enhanced anti-cancer efficacy and establishes long-term immune memory protection (Fig. 1). In conclusion, we have proposed a safe and versatile therapeutic strategy with great potential in the clinical treatment of "cold" tumors.

2. Materials and methods

2.1. Materials

Lactide: glycolide (50: 50) (PLGA, wt: 38,000−54,000), poly (vinyl alcohol) (PVA, 86% 89% hydrolyzed, low molecular weight); 1,2-dioleoyl-3-trimethylammonium propane (DOTAP) (95%) were purchased from RuiXi Biochemical Co., Ltd. Diethyldithiocarbamic acid silver salt (Ag (DDTC), 98%) was bought from Aladdin Industrial Co., Ltd. Sodium polyoxotungstate (POM1) was purchased from MCE Co., Ltd. Octadecene (ODE, 95%) was purchased from Macklin Biochemical Co., Ltd. 2,2,6,6-tetramethylpiperidine (TEMP, 95%), and 2,7-dichlorofluorescin diacetate (DCFH-DA, 97%) were purchased from Sigma−Aldrich Co., Ltd. Singlet Oxygen Sensor Green (SOSG), Mitochondrial membrane potential assay kit with JC-1, Reactive Oxygen Species Assay Kit, Membrane and Cytosol Protein Extraction Kit was purchased from Beyotime Biotechnology Co., Ltd. FITC Annexin V Apoptosis Detection Kit was purchased from BD Biosciences Co., Ltd. All antibodies used in flow cytometry were purchased from Biolegand Biosciences Co., Ltd. All the reagents used in the experiment were the analytical and used directly without treatment.

2.2. Preparation of Ag_2S QDs, QD@NP@M, and QD/POM1@NP@M

Ag_2S QDs were synthesized according to our previous method. QD@NP and QD/POM1@NP were synthesized utilizing the double-emulsion technique. For the preparation of QD/POM1@NP, POM1 (5 mg) was dissolved in 100 μL of water as the aqueous phase. Subsequently, 60 mg of PLGA and 5 mg of DOTAP were dissolved in 2 mL dichloromethane (DCM), and

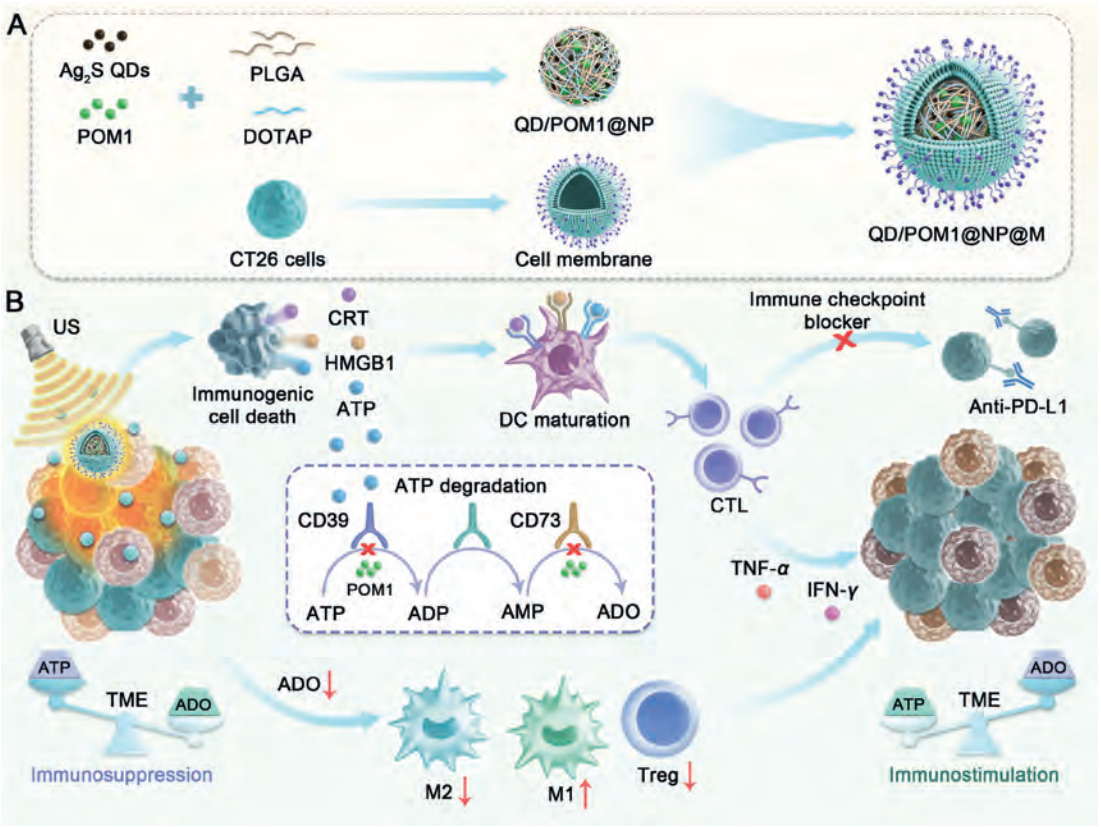

Figure 1 Schematic diagram of metabolic reprogramming nanomedicines potentiate sonodynamic immunotherapy by inhibiting the CD39/CD73/ADO pathway. (A) The synthesis route of QD/POM1@NP@M. (B) The mechanisms of sonodynamic immunotherapy mediated by QD/POM1@NP@M. Following intravenous injection, QD/POM1@NP@M targets the tumor *via* a homologous cell membrane. Upon exposure to US irradiation, the nanoparticles induce immunogenic cell death, characterized by the release of CRT, HMGB1, and ATP. This process promotes the maturation of DCs, which subsequently activate cytotoxic T lymphocytes to secrete cytokines and exert anti-tumor effects. Concurrently, the CD39 inhibitor POM1, released from the nanoparticles, mitigates adenosine accumulation, thereby diminishing the immunosuppressive effects of ADO. This reduction in ADO levels leads to a decrease in M2-TAMs and Tregs while increasing the population of M1-TAMs.

500 μL Ag_2S QDs solution was added to 2 mL DCM (organic phase). The aqueous phase was then slowly added to the organic phase, followed by ultrasound treatment in an ice bath for 2 min at 25% power. After the ultrasound, the emulsion was added dropwise into 4 mL of 2.5% PVA solution, and the ultrasound was repeated ice bath for 1 min at 25% power. Subsequently, 36 mL of ultra-pure water and 4 mL of 2.5% PVA solution were added before introducing 50 mL of ultra-pure water. The removal of DCM was carried out using a rotary evaporator. The resulting solution was then centrifuged at 12,000 rpm for 15 min. Following twice washing steps, the precipitate was resuspended in 500 μL of ultra-pure water, stored at −80 °C, and freeze-dried for preservation. The synthesis of QD@NP follows the same steps as QD/POM1@NP except that the POM1 solution was not added.

The Membrane Protein Extraction Kit was utilized for the isolation of the cell membrane from CT26 cells. In the process of synthesizing QD/POM1@NP@M, a mixture of cell membranes (1 mg/mL) and QD/POM1@NP (2 mg/mL) was stirred on ice for 1 h. Subsequently, the resulting mixture was extruded through 400 and 200 nm pore-size filter membranes using an Avanti mini-extruder for a total of 10 extrusions.

2.3. Characterization of Ag_2S QDs, QD@NP@M, and QD/POM1@NP@M

The morphology and sizes of QD@NP@M and QD/POM1@NP@M were captured using a transmission electron microscope (FEI Tecnai G2 F30). The hydrated particle size and zeta potential of QD@NP@M and QD/POM1@NP@M were measured by Malvern Zetasizer Apparatus (Worcestershire, UK). ESR spectra were measured by CIQTEK EPR200M with continuous-wave X band frequency.

The levels of membrane proteins contained in the nanoparticles were detected by SDS-PAGE. Cell lysates, cancer cell membranes, and QD/POM1@NP@M protein concentrations were determined using the BCA Protein Assay Kit. Protein extracts were mixed with 5 × SDS-PAGE sample uploading buffer, boiled at 95 °C for 10 min, and loaded onto 10% SDS-PAGE gels for electrophoresis. The gel was then stained with Coomassie Brilliant Blue for 1 h and washed repeatedly with Coomassie Blue Staining Destaining Solution until the background was colorless. Finally, the gel was photographed and analyzed for protein bands.

The production of single linear oxygen ($^1O_2$) by QD/POM1@NP@M after US irradiation was initially determined by electron spin resonance (ESR). 50 μL of TEMP was added to 1 mL of QD/POM1@NP@M (100 μg/mL). After US irradiation in the dark (1 W/cm^2, 3 min)), the ESR spectra of TEMP were monitored to quantify the rate of $^1O_2$ production. For comparison, the effects of TEMP + US, and TEMP + QD/POM1@NP@M on $^1O_2$ generation were also evaluated.

Furthermore, the utilization of SOSG facilitated the quantitative assessment of $^1O_2$ levels generated by QD/POM1@NP@M following ultrasound irradiation. QD/POM1@NP@M (200 μg/mL) and SOSG solution (5 μmol/L) were sonicated (1.5 W/cm^2) at different times and then the fluorescence intensity of the resulting mixtures was quantified.

2.4. Cell culture and animals

Murine colon cancer cell line CT26 and human colorectal adenocarcinoma cell lines Caco-2 were purchased from the American Type Culture Collection (ATCC), USA. CT26 cells were cultured in RPMI-1640 medium supplemented with 10% fetal bovine serum (FBS) and 1% antibiotics (penicillin/streptomycin, 10,000 U/mL), while Caco-2 cells were cultured in DMEM medium with 10% FBS and 1% antibiotics. Both cell lines were incubated at 37 °C under a 5% carbon dioxide (CO_2) atmosphere.

Balb/c mice aged 6−8 weeks were housed in an environment set at a temperature of 22 ± 2 °C, with 50%−55% relative humidity, and a 12-h light−dark cycle. All mice had unrestricted access to food and water throughout the experiment. The experimental procedures strictly adhered to the guidelines provided by the Department of Laboratory Animal Management and the Ethics Committee of Xi'an Jiao Tong University.

2.5. In vitro therapeutic effects

The therapeutic effect *in vitro* of QD/POM1@NP@M was elucidated by ROS assay, apoptosis assay, MMP assay, and Calcein-AM/PI staining assay. CT26 cells were inoculated in 12-well plates at a density of 1×10^5/well. After overnight adherence, the cells were incubated with different materials (200 μg/mL) for 8 h. Subsequently, the cells were washed with PBS and the cells in the radiation group were exposed to ultrasound irradiation (1 W/cm^2, 3 min). Cells were subjected to staining with DCFH-DA for the ROS assay and Calcein-AM/PI staining for the live-dead assay immediately after ultrasound irradiation. The staining process lasted 30 min, followed by imaging and analysis. MMP assay was performed by staining the cells with the JC-1 probe for 20 min at 3 h after sonication. Subsequently, cell images were captured using fluorescence microscopy and intracellular JC-1 fluorescence intensity was quantified by flow cytometry. To assess apoptosis, cells were harvested 6 h after sonication exposure, stained with Annexin V-FITC and PI, and then analyzed by flow cytometry.

2.6. Assessment of cellular ICD status

In vitro ICD inducibility was evaluated by characterizing CRT, HMGB1 expression, and ATP secretion. CT26 cells were incubated with different nanoparticles (200 μg/mL) for 8 h. The irradiated group was washed with PBS and then irradiated with ultrasound (1 W/cm^2, 3 min). The treated cells were further incubated for 24 h. Cells and media were collected and intracellular and extracellular ATP levels were measured using an ATP luciferase-based quantification kit (Beyotime, S0026) according to the method provided by the manufacturer. The specific steps are as follows: Add 200 μL of lysate to each well of a 6-well plate and mix thoroughly to lyse the cells. The cells are then centrifuged at 12,000×*g* for 5 min at 4 °C and the supernatant is removed for subsequent assays. Add 100 μL of ATP assay working solution to the assay wells and allow to stand at room temperature for 3−5 min to deplete background ATP. 20 μL of sample or standard is then added to the assay wells and mixed quickly with a micropipette, and the fluorescence intensity is measured with a luminometer after 10 s. Meanwhile, the cells were stained with anti-CRT (Proteintech, Cat No. 10829-1-AP) or anti-HMGB1 (Proteintech, Cat No. 10829-1-AP) primary antibody and Fluor 488 secondary antibody after fixing with 4% paraformaldehyde. Finally, the expression of CRT and HMGB1 on CT26 cells was observed using fluorescence microscopy.

2.7. Assessment of mature DC

Bone marrow-derived dendritic cells (BMDCs) were obtained based on methods reported in the literature[27]. BMDCs were isolated

from the 6- to 8-week-old female Balb/c mice. The isolated cells were then induced to differentiate using a BMDCs medium composed of RPMI-1640 supplemented with 1% penicillin−streptomycin, 10% fetal bovine serum (FBS), interleukin-4 (IL-4) at a concentration of 10 ng/mL, and granulocyte-macrophage colony-stimulating factor (GM-CSF) at 20 ng/mL. The differentiation process lasted for six days. Then, CT26 cells were seeded into the upper chamber of the Transwell system, incubated overnight, and then incubated with different nanoparticles (200 μg/mL) for an additional 8 h. After removing the nanoparticles, the CT26 cells were washed twice with PBS. Then, the irradiated group was subjected to ultrasound irradiation (1 W/cm^2, 3 min). Finally, the extracted BMDCs were inoculated into the lower layer of the transwell system and co-cultured with treated CT26 cells for 24 h. BMDCs from the bottom layer were collected and the proportion of mature BMDCs ($CD11c^+CD80^+CD86^+$) was analyzed by flow cytometry after staining with FITC anti-CD11c, APC anti-CD80, and PE anti-CD86 antibodies.

2.8. Assessment of biocompatibility

In vitro, biocompatibility was evaluated by MTT assay. CT26 cells were inoculated in 96-well plates (1×10^4 cells/well) and incubated with different concentrations of QD/POM1@NP@M (0−400 μg/mL) for 24 or 48 h after allowing the cells to attach to the wall overnight. Cells were washed with PBS and MTT was added and the cells continued to be incubated for 4 h. Then, the crystalline violet precipitate generated by the cells was solubilized with DMSO, and the absorbance was measured at 570 nm to calculate the cell viability.

For *in vivo* evaluation of biocompatibility, fifteen mice were divided into three groups, two of which were injected with QD/POM1@NP@M (5 mg/kg based on POM1) through the tail vein four times every four days, and the other group was injected with PBS. Mice were executed on Days 15 or 30, and blood was collected for routine blood analysis and blood biochemical indexes. At the same time, major organs (heart, liver, spleen, lung, and kidney) of mice were collected for tissue section H&E staining to assess organ integrity.

2.9. In vivo fluorescent imaging

After the construction of the mouse subcutaneous colon cancer model, 100 μL DiR-labeled nanoparticles were injected intravenously into mice when the tumor volume reached 200 mm^3. *In vivo*, fluorescence images of mice were acquired using the IVIS imaging system at 0, 0.5, 1, 3, 6, 9, 12 and 24 h after injection. Meanwhile, mice were executed after *in vivo* imaging, and major organs (heart, liver, spleen, lungs, and kidney) and tumors were collected for *ex vivo* imaging to study the tissue distribution of nanoparticles.

2.10. In vivo anti-tumor effect

The tumor model of mice was established by subcutaneous injection of CT26 cells (2×10^6) suspended in PBS (100 μL) into the right rear region of the back of mice. When the tumor volume reached 100 mm^3, the mice were randomly divided into the following six groups as follows: G1: Control, G2:US, G3: QD@NP@M, G4: QD@NP@M+US, G5: QD/POM1@NP@M, and G6: QD/POM1@NP@M+US Nanoparticles (5 mg/kg based on POM1) were injected through a tail vein followed by ultrasound irradiation four times every four days. Ultrasound irradiation was performed at 3 h after injection. The body weight and tumor volume of mice were recorded every 2 days. Tumor volume was calculated according to Eq. (1):

$$V = \text{Width}^2 \times \text{Length}/2 \quad (1)$$

After 15 days, mice were executed, and tumors and major organs were collected for further analysis. Tumors were photographed, and then organs and tumors were sectioned and examined histopathologically under a microscope.

2.11. Immune cell analysis

Single-cell suspensions were prepared from differently treated tumor tissues for flow cytometry analysis. Tumor tissues were cut into small pieces and incubated in dissociation buffer (100 μg/mL deoxyribonuclease I and 1 mg/mL collagenase IV) at 37 °C for 60 min to obtain single-cell suspensions. Single-cell suspensions were washed with PBS buffer and then stained with the following antibodies: APC/Cyanine7 anti-CD45, PE/Cyanine7 anti-CD8a, FITC anti-CD11b, PerCP/Cyanine5.5 anti-CD11c, Pacific Blue™ anti-CD4, PE anti-TNF-α, APC anti-IFNγ, PE anti-Foxp3, APC anti-CD39, PE anti-CD206. The cell suspension was analyzed by flow cytometry at the end of staining. The subsequent analysis was conducted using Flowjo software to determine the proportions of the following cell populations: Tregs ($CD45^+CD4^+Foxp3^+$), M1-like TAMs ($CD45^+CD11b^+CD86^+$), M2-like TAMs ($CD45^+CD11b^+CD206^+$), CD8 T cells ($CD45^+CD8+$), and CD8 T cells ($CD45^+CD8^+$).

2.12. SDT plus PD-L1 blockade combination therapy

The tumor model of mice was established by subcutaneous injection of CT26 cells (2×10^6) suspended in PBS (100 μL) into the right rear region of the back of mice. When the tumor volume reached 100 mm^3, the mice were randomly divided into the following four groups as follows: G1: Control, G2: α-PDL1, G3: QD/POM1@NP@M+US, G4: QD/POM1@NP@M+US+α-PDL1. QD/POM1@NP@M nanoparticles (5 mg/kg based on POM1) were administered to mice in G3 and G4 *via* tail vein injection on Days 0, 4, 8, and 12. Subsequently, mice in the G2 and G4 experimental groups were treated with 150 μg of α-PD-L1 antibody (BioXcell, Cat No. BE0101) intraperitoneally on Days 1, 4, 7, and 10. After a 6-h interval post-injection, the mice were exposed to ultrasound irradiation (1.5 W/cm^2, 3 min). The mice's body weight and tumor volume were recorded every other day. Tumor volume was calculated according to Eq. (1). At the end of treatment, tumors, and spleens of mice were collected for section staining or flow cytometry analysis.

2.13. Statistical analysis

All data were analyzed using GraphPad Prism 9.0 software. The data obtained are expressed as mean ± standard deviation (SD) with no less than three replications for each experiment. Statistical comparisons between groups were calculated by Student's *t*-test and ANOVA test. Reported *P*-values: $^{***}P < 0.001$, $^{**}P < 0.01$, $^{*}P < 0.05$ were considered statistically significant.

3. Results and discussion

3.1. CD39 expression and immune cell infiltration in colon adenocarcinoma

The findings have demonstrated a significant correlation between elevated CD39 expression and a suppressive TME, indicating that CD39 may serve as a promising therapeutic target[28]. The composition of immune cells within the TME is intricately associated with cancer prognosis and treatment response. To explore this relationship, we investigated the correlation between the expression of CD39 and immune cell infiltration in colon adenocarcinoma (COAD). The results demonstrate a significant positive correlation between CD39 expression and the prevalence of pro-tumor immune cells, including Tregs and M2-like TAMs, within the tumor microenvironment (Fig. 2A). A pivotal component of an effective anti-tumor immune response is the predominance of $CD8^+$ T cells. Importantly, existing research indicates that $CD39^+CD8^+$ T cells are frequently associated with a state of immune exhaustion[29,30]. Furthermore, the results indicate a positive correlation between CD39 expression and the infiltration of CD8 T cells and CD4 T cells within the TME (Fig. 2B). Additionally, a strong association was observed between CD39 expression and the expression of immune exhaustion-related genes such as PD-1 and TIM-3 (Fig. 2C). These findings suggest that targeting CD39 expression in colon cancer TME may represent a viable therapeutic strategy to mitigate the immunosuppressive characteristics of the TME and enhance the efficacy of the immune response.

3.2. Synthesis and characterization of QD/POM1@NP@M

Firstly, Ag_2S QDs were synthesized according to the previous method developed in our lab[31]. Secondly, PLGA-based polymer nanocarrier was synthesized by double microemulsion technique to achieve simultaneous encapsulation of hydrophobic Ag_2S QDs and hydrophilic drug POM1 (QD/POM1@NP). Thirdly, homologous tumor cell membranes were coated on QD/POM1@NP to synthesize biomimetic nanocarriers (QD/POM1@NP@M) to enhance the targeting ability of the nanocarriers and prolong their *in vivo* circulation time. Representative transmission electron microscope (TEM) images showed that the Ag_2S QDs have a uniform particle size of about 4 nm. The QD/POM1@NP showed a uniformly sized spherical shape in which Ag_2S QDs are visible as black dots. The QD/POM1@NP@M surface showed a clear lamellar film (Fig. 3A). Elemental mapping images showed that Ag, S, and W elements were uniformly distributed inside the nanocarriers, indicating that the Ag_2S QDs and POM1 were successfully encapsulated in the PLGA-based nanocarrier (Fig. 3B). We also measured the drug encapsulation efficiency (EE) of Ag_2S QDs and POM1 by ICP−MS, which were 82.3% ± 5.43% and 18.2% ± 1.75%, respectively, suggesting the effective encapsulation of them in QD/POM1@NP. The dynamic light scattering (DLS) analysis revealed that the zeta potential of QD/POM1@NP was approximately −8.2 ± 0.1 mV, with a hydrated particle size of around 212.4 ± 3.5 nm (Fig. 3C and D). The QDs/POM1@NP@M exhibited a lower zeta potential of −22.7 ± 0.3 mV and a larger hydrated particle size of approximately 226.5 ± 2.5 nm following cell membrane wrapped (Fig. 3C and D). SDS-PAGE analysis showed that the protein bands of the QD/POM1@NP@M group (III) were consistent with that of the cell membrane (II) (Fig. 3E). The above results indicated that the cell membrane had been successfully wrapped around the PLGA-based nanocarrier, suggesting that the metabolic reprogramming nanomedicines were successfully synthesized.

Our previous work demonstrated that Ag_2S QDs are novel sonosensitizers. Sonodynamic effects of Ag_2S QDs were detected by electron spin resonance (ESR) using the single linear oxygen ($^1O_2$) trapping agent 2,2,6,6-tetramethylpiperidine (TEMP). ESR

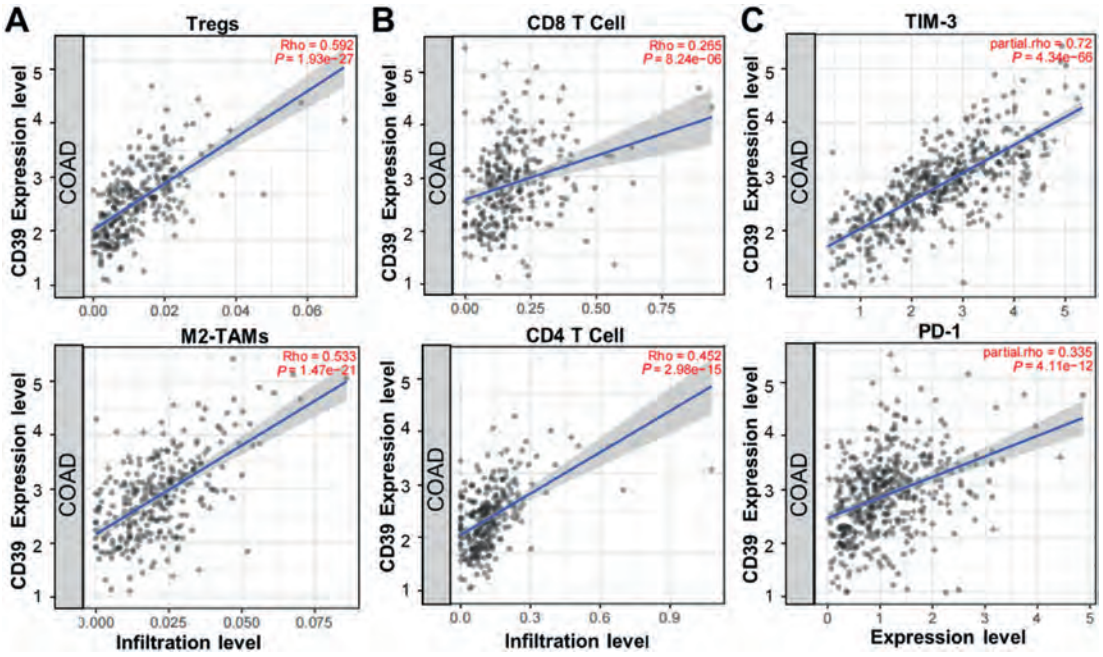

Figure 2 CD39 expression and immune cell infiltration in colon adenocarcinoma (COAD). (A) The correlations between the expression of CD39 and the infiltration of Tregs and M2-like TAMs in COAD tissues. (B) The correlations between the expression of CD39 and the infiltration of CD8 and CD4 T cells in COAD tissues. (C) The correlations between the expression of CD39 and the expression of TIM-3 and PD-1 in COAD tissues.

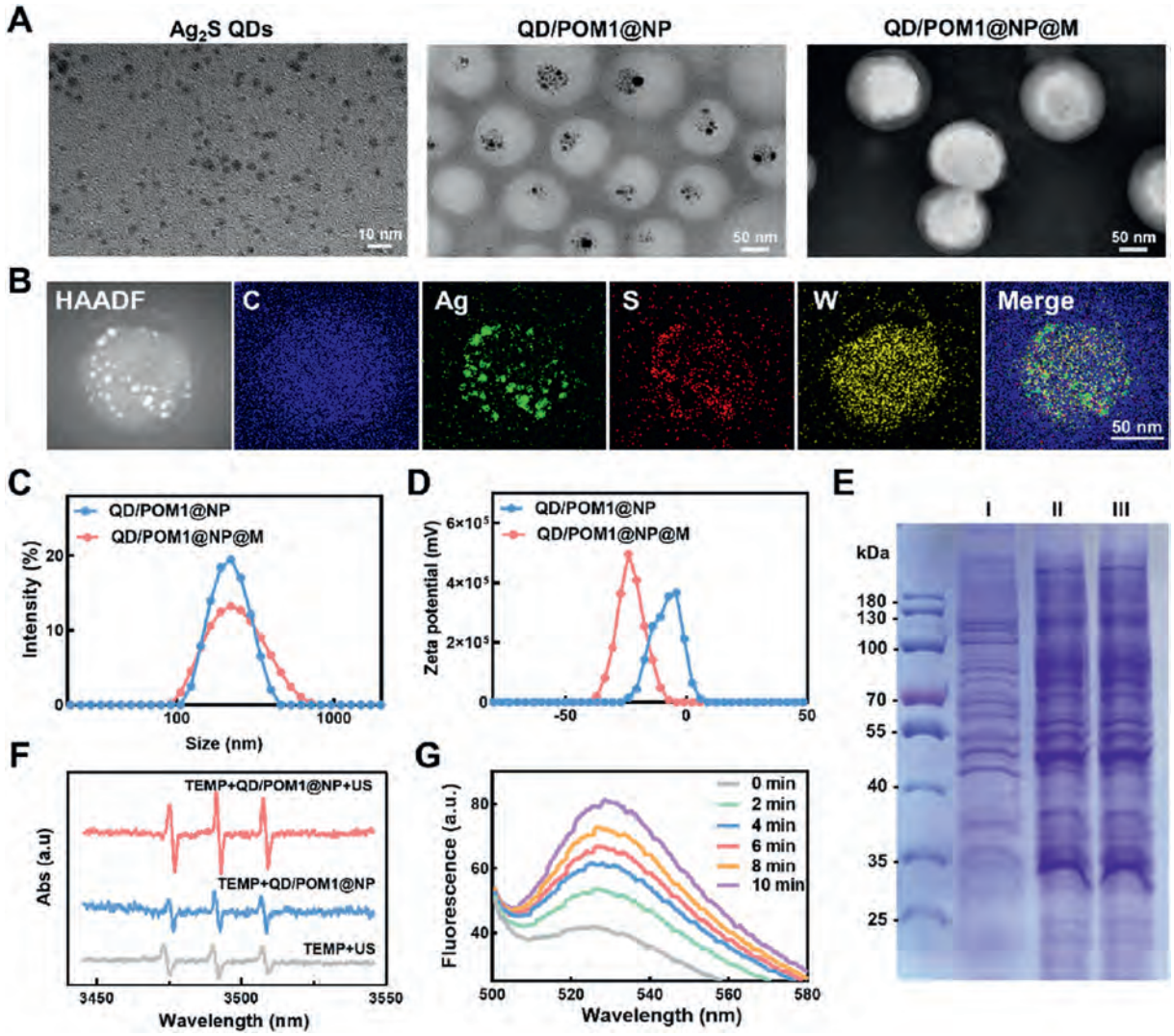

Figure 3 Characterization of QD/POM1@NP@M. (A) TEM images of Ag_2S QDs, QD/POM1@NP, and QD/POM1@NP@M, scale bar = 10 or 50 nm. (B) Element mapping images of QD/POM1@NPs, scale bar = 50 nm. (C) Size distribution of QD/POM1@NP, and QD/POM1@NP@M measured by DLS. (D) Zeta potential of QD/POM1@NP, and QD/POM1@NP@M measured by DLS. (E) SDS-PAGE image. I: cell lysate, II: cancer cell membrane, III: QD/POM1@NP@M. (F) $^1O_2$ produced by QD/POM1@NP@M under different treatments was detected by ESR (Ultrasonic parameter: 1.5 W/cm^2, 3 min) (G) $^1O_2$ produced by QD/POM1@NP@M after different ultrasonic irradiation time was detected by SOSG (Ultrasonic parameter: 1.5 W/cm^2).

results showed that the QD/POM1@NP@M + TEMP + US group produced a higher $^1O_2$ characteristic signal compared to the unstimulated and control groups, indicating the highest production of $^1O_2$ (Fig. 3F). Then, the $^1O_2$-specific fluorescent probe Singlet Oxygen Sensor Green (SOSG) was further utilized to verify its sonodynamic effect. With the prolongation of ultrasonic irradiation time, the fluorescence intensity of SOSG gradually increased (Fig. 3G). Taken together, these results indicate that the QD/POM1@NP@M exhibit excellent sonodynamic properties due to the successful integration of Ag_2S QDs within them.

The stability of nanoparticles is a crucial factor for their biological applications. To assess the stability of QD/POM1@NP@M, they were dispersed in various solutions (water, PBS, and RPMI 1640 medium with 10% FBS), and the changes in particle size were measured over time. As illustrated in Supporting Information Fig. S1, both the size and polydispersity index (PDI) of the QD/POM1@NP@M remained relatively stable over a 7-day period. These results indicate that the QD/POM1@NP@M NPs exhibit excellent stability.

3.3. *In vitro therapeutic effects of QD/POM1@NP@M*

Efficient cellular uptake of nanomedicines is crucial for the successful implementation of SDT. To determine the optimal sonication duration, we investigated the endocytosis of nanoparticles by labeling them with the fluorescent probe DiL (DiL@NP@M), and subsequently incubating them with CT26 cells. Fluorescence images demonstrated a time-dependent increase in intracellular fluorescence intensity, with a significant accumulation of red fluorescent nanoparticles observed within the cytoplasm of CT26 cells after 8 h of co-culture (Supporting Information Fig. S2A). These findings were further corroborated by flow cytometry analysis, reinforcing the conclusion that nanoparticles can be effectively taken up by CT26 cells (Fig. S2B−S2D). It is

currently believed that the main mechanism of SDT is to cause cell death by generating ROS[32]. Therefore, the ROS levels of cells after different treatments were first examined using the fluorescent probe fluorescent 2′,7′-dichlorofluorescein diacetate (DCFH-DA). The analysis of the fluorescent photographs revealed minimal green fluorescence in the control, QD@NP, and QD/POM1@NP@M groups, with only a slight increase observed in the US group. Conversely, the groups exposed to Ag_2S QDs under ultrasound stimulation (QD@NP@M + US, QD/POM1@NP@M + US) exhibited pronounced green fluorescence. This indicates that the sonosensitizers Ag_2S QDs generate substantial quantities of ROS when subjected to ultrasound (Fig. 4A). Flow cytometry and quantitative fluorescence statistics also showed that the group in which Ag_2S QDs were present had the largest percentage of cells positive for green fluorescence and the strongest fluorescence (Fig. 4B and C). Excessive ROS compromise the mitochondrial respiratory chain and degrade the mitochondrial membrane structure, resulting in the loss of mitochondrial membrane potential (MMP)[33]. Subsequently, the MMP of CT26 cells subjected to various treatments was assessed using the fluorescence probe, JC-1. CT26 cells in the control, QD@NP@M, and QD/POM1@NP@M groups exhibited bright red fluorescence. In contrast, cells in the QD@NP@M + US and QD/POM1@NP@M + US groups displayed strong green fluorescence, suggesting that ultrasonic irradiation resulted in the loss of MMP in these two groups. Consequently, JC-1 was converted to its monomeric form, which emits green fluorescence (Fig. 4D). Flow cytometry results also showed a significant decrease in cell MMP after ultrasonic irradiation, with the most pronounced decrease in the QD/POM1@NP@M + US group (Fig. 4E and Supporting Information Fig. S3A). The loss of mitochondrial transmembrane potential constitutes an irreversible event during the early stages of apoptosis[34]. This decline in the potential difference across the mitochondrial membrane triggers the release of apoptotic factors, initiating a cascade of apoptotic responses that culminate in cell death. Subsequently, apoptosis was evaluated

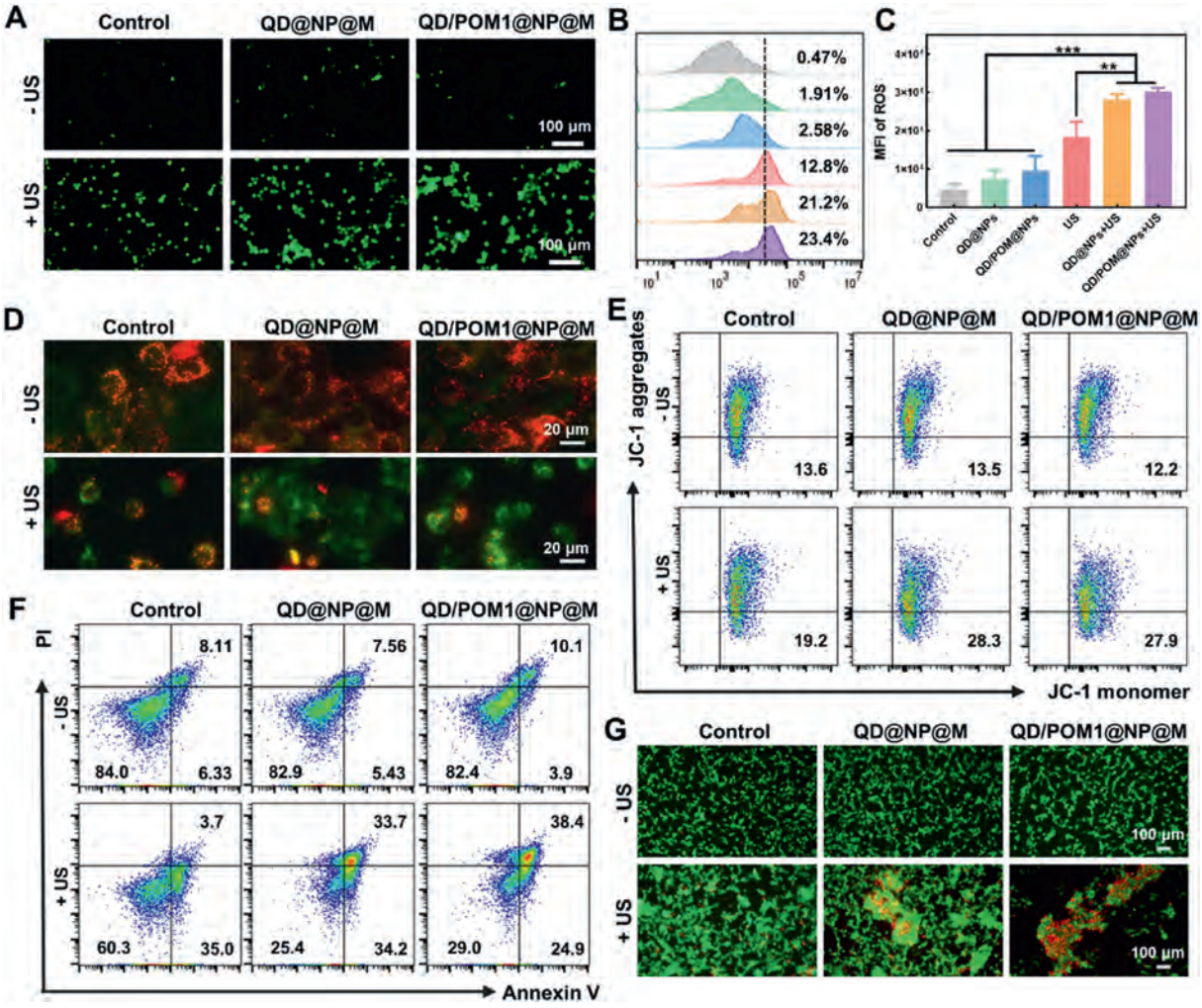

Figure 4 *In vitro* therapeutic effects of QD/POM1@NP@M. (A) Fluorescence images of DCFH-DA staining of CT26 cells after various treatments. Scale bar = 100 μm. (B) ROS levels in CT26 cells after different treatments were detected by flow cytometry. (C) The corresponding fluorescence intensity of DCFH-DA in CT26 cells after different treatments. (D) MMP of CT26 cells under different treatments was assessed by JC-1 using fluorescent staining. Scale bar = 20 μm. (E) MMP of CT26 cells under different treatments was assessed by JC-1 using flow cytometry. (F) Apoptosis of CT26 cells was assessed by Annexin V-FITC/PI staining using flow cytometry. (G) Fluorescence images of Calcein-AM/PI staining of CT26 cells after different treatments. Scale bar = 100 μm. Data are presented as mean ± SD. ($n = 3$). P values were determined using a one-way ANOVA test or Student's t-test. Statistically significant difference: $^*P < 0.05$, $^{**}P < 0.01$, $^{***}P < 0.001$.

through Annexin V/PI staining of cells subjected to various treatments. Consistent with the aforementioned results, the QD/POM1@NP@M + US group exhibited the highest rate of CT26 cell apoptosis (64% ± 3.4%) compared to the other groups (Fig. 4F and Fig. S3B). Furthermore, the cytotoxicity of the various treatments was assessed using Calcein-AM/PI staining. As depicted in Fig. 4G, the red fluorescent signal was scarcely detectable in the US group, QD@NP@M group, and QD/POM1@NP@M group, indicating that the majority of the cells remained viable post-treatment. In contrast, the QD/POM1@NP@M + US group demonstrated the most intense red fluorescence among all groups, signifying the highest efficacy in inducing tumor cell apoptosis.

3.4. In vitro immunogenic cell death triggered by QD/POM1@NP@M

SDT can induce ICD, thereby releasing damage-associated molecular patterns (DAMPs) signals such as CRT, HMGB1, and ATP along with tumor-associated antigens (TAAs), recruiting lymphocytes and activating anti-tumor immune responses[18]. To investigate whether QD/POM1@NP@M can effectively initiate ICD and promote DAMPs release, we assessed the expression of ICD markers *in vitro*. Visualization analysis of CRT and HMGB1 expression in CT26 cells after different treatments was conducted using fluorescence microscopy. Results indicated that the expression of CRT in the QD@NP@M+US and QD/

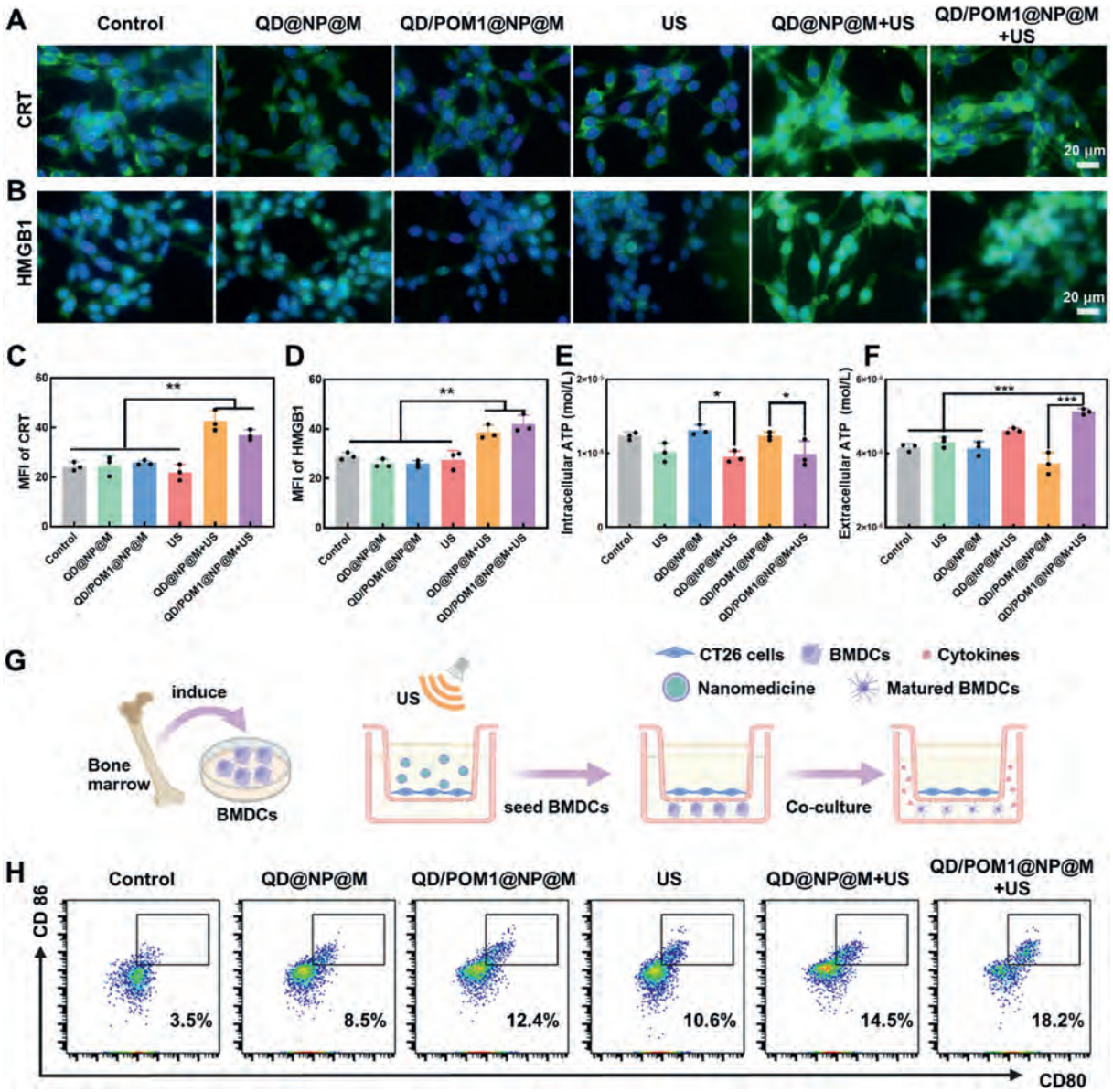

Figure 5 *In vitro* immunogenic cell death triggered by QD/POM1@NP@M. (A, B) Immunofluorescence staining images of (A) CRT and (B) HMGB1 expression in CT26 cells after different treatments. Scale bar = 20 μm. (C, D) The corresponding fluorescence intensity of (C) CRT and (D) HMGB1 is shown in Fig. 2A and B. ($n = 3$). (E, F) (E) Intracellular and (F) extracellular ATP levels in CT26 after different treatments. (G) The design scheme of the BMDCs maturation experiment. (H) Effect of tumor cells treated with different treatments on BMDCs maturation. Data are presented as mean ± SD. *P* values were determined using a one-way ANOVA test or Student's *t*-test. Statistically significant difference: $^{*}P < 0.05$, $^{**}P < 0.01$, $^{***}P < 0.001$ (Fig. 5G produced from bioRender.com, with permission).

POM1@NP@M+US groups was higher compared to other groups (Fig. 5A). Particularly, the QD/POM1@NP@M+US group exhibited higher CRT expression, with a 1.52-fold increase in intracellular CRT fluorescence intensity compared to the control group (Fig. 5C). Further observations revealed a significant upregulation of HMGB1 in the QD@NP@M+US group and QD/POM1@NP@M + US, with fluorescence intensity increased by 1.33- and 1.44-fold compared to the US groups, respectively (Fig. 5B and D). Furthermore, the levels of intracellular and extracellular ATP in cells after different treatments were examined. In the QD@NP@M+US and QD/POM1@NP@M+US group, a decrease in intracellular ATP levels in CT26 cells was observed, while an increase in ATP levels in the supernatant. It indicated that ultrasound treatment resulted in partial cell death, leading to the release of ATP into the extracellular space (Fig. 5E and F). The ATP released by tumor cells during ICD functions as a pivotal "find me" signal, orchestrating the infiltration of immune effector cells. Following treatment with QD/POM1@NP@M combined with US, the extracellular ATP concentration reached its peak, thereby facilitating the recruitment of a greater number of immune cells to the tumor site and subsequently initiating the host's immune response (Fig. 5F).

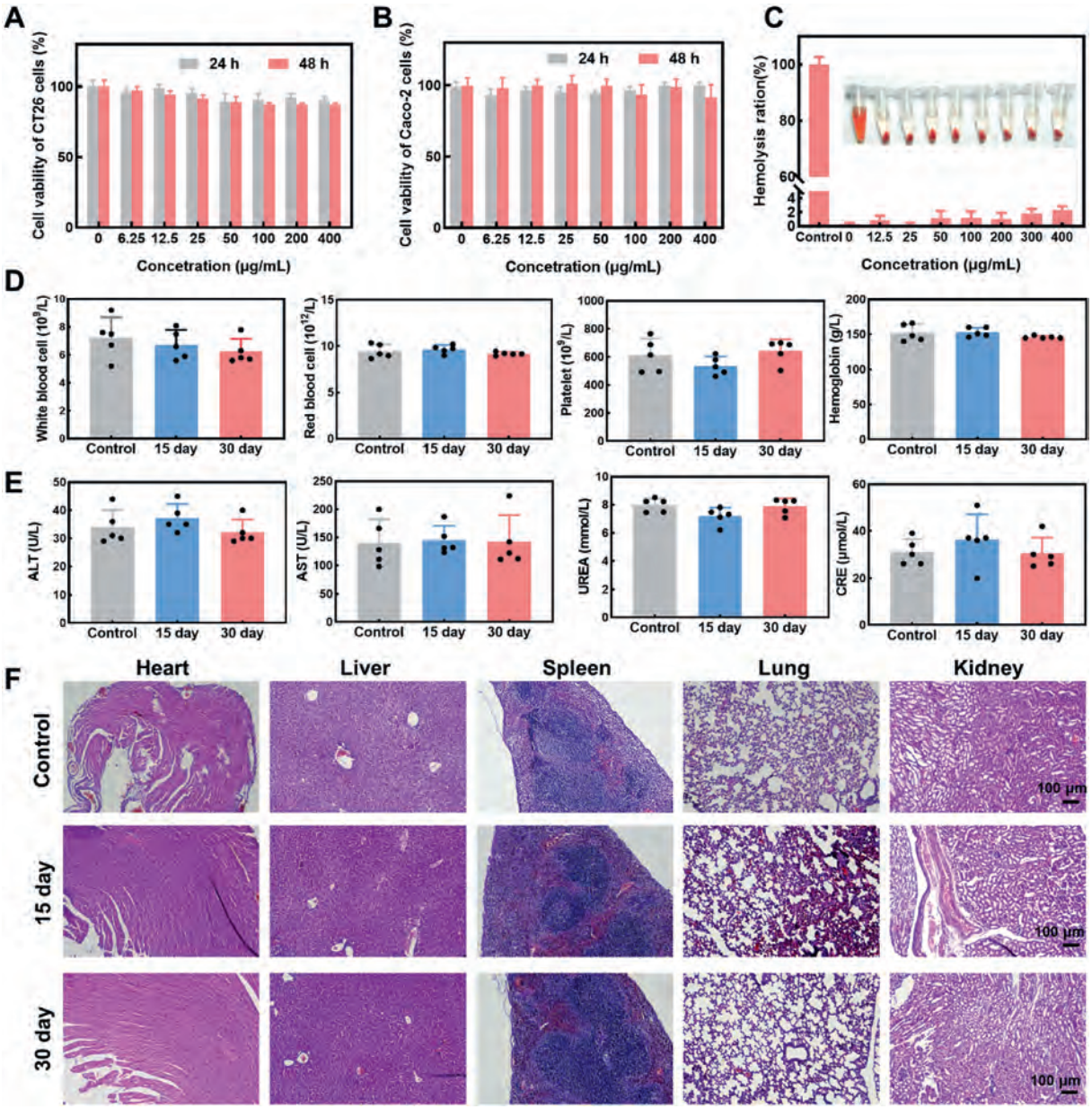

Figure 6 Biocompatibility of QD/POM1@NP@M. (A, B) The cell viability of CT26 cells (A) and Caco-2 cells (B) treated with different concentrations of QD/POM1@NP@M for 24 and 48 h ($n = 5$). (C) Hemolysis rate of blood cells co-incubated with different concentrations of QD/POM1@NP@M for 6 h. (D, E) (D) The routine blood test parameters and (E) biochemical parameters of the blood of mice following three injections of QD/POM1@NP@M or saline for 15 and 30 days ($n = 5$). (F) The H&E staining images of mice organs after three injections of QD/POM1@NP@M or saline for 15 and 30 days. Data are presented as mean ± SD. P values were determined using a one-way ANOVA test or Student's t-test. Statistically significant difference: $^{*}P < 0.05$, $^{**}P < 0.01$, $^{***}P < 0.001$.

The substantial release of DAMPs during ICD can stimulate dendritic cells (DCs) maturation, thereby further promoting the activation, proliferation, and tumor infiltration of cytotoxic T lymphocytes (CTLs)[20]. Subsequently, the efficacy of ICD under different conditions was assessed by determining the maturation levels of bone marrow-derived dendritic cells (BMDCs) *in vitro*. BMDCs were co-cultured with CT26 cells treated differently, and after 24 h, the maturation level of BMDCs was evaluated. The design scheme of the BMDCs maturation experiment is shown in Fig. 5G. As expected, when BMDCs co-cultured with CT26 cells irradiated by US only, the proportion of mature DCs ($CD11C^{+}CD80^{+}CD86^{+}$) slightly increased compared to the control group. The maturation of BMDCs in the QD@NP@M+US group further increased to 14.4% ± 0.4%, with the highest average BMDCs maturation rate observed in the QD/POM1@NP@M+US group at 18.3% ± 0.5% (Fig. 5H and Supporting Information Fig. S4). The findings suggest that the activation of BMDCs in the QD/POM1@NP+US group is the

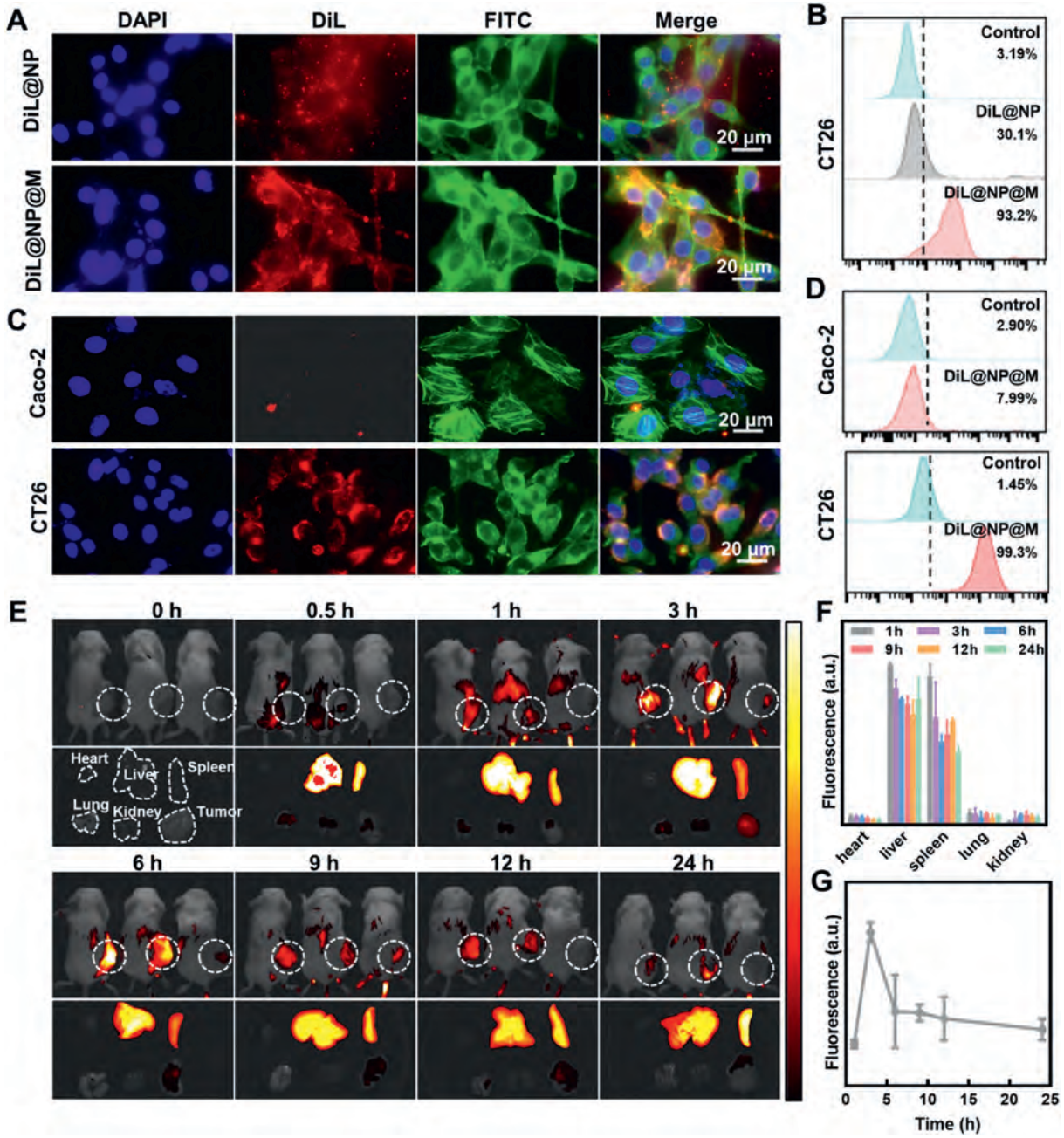

Figure 7 Biodistribution of QD/POM1@NP@M. (A, B) (A) Fluorescence image and (B) flow cytometry analysis of CT26 cells incubated with DiL@NP and DiL@NP@M at 8 h. Scale bar = 20 μm. (C, D) (C) Fluorescence image and (D) flow cytometry analysis of Caco-2 cells and CT26 cells incubated with DiL@NP@M at 8 h. Scale bar = 20 μm. (E) Fluorescence images of CT26 tumor-bearing mice, organs, and tumors at indicated time points after injection of QD/POM1@NP@M. (F) Quantification of fluorescence intensity of major organs at different time points after tail vein injection of QD/POM1@NP@M (G) Quantification of fluorescence intensity of tumor at different time points after tail vein injection of QD/POM1@NP@M. Data are presented as mean ± SD.

most efficacious, highlighting the synergistic effects of SDT and POM1. These results substantiate that SDT can effectively induce ICD and that the DAMPs released by ICD, in conjunction with POM1, collectively enhance DC maturation, thereby initiating host anti-tumor immunity.

3.5. *Biocompatibility of QD/POM1@NP@M*

The biocompatibility of the QD/POM1@NP@M was further evaluated, laying the groundwork for subsequent *in vivo* therapies. First, the toxicity of different concentrations of the QD/POM1@NP@M on CT26 cells and Caco-2 cells was evaluated at the cellular level through an MTT assay. The results demonstrated that after incubation with 400 μg/mL QD/POM1@NP@M for 24 h (Fig. 6A) and 48 h (Fig. 6B), the majority of CT26 cells and Caco-2 remained viable. In addition, hemolysis assay results showed that the hemolysis rate of 400 μg/mL QD/POM1@NP@M was still minimal after 6 h of incubation with blood cells (Fig. 6C). Subsequently, the biocompatibility of the QD/POM1@NP@M was further evaluated in mice. Blood and organs from the mice were collected 15 and 30 days after intravenous injection of the QD/POM1@NP@M for biocompatibility evaluation. Routine blood tests showed no significant difference between the PBS-treated group and the drug-treated group at 15 and 30 days after

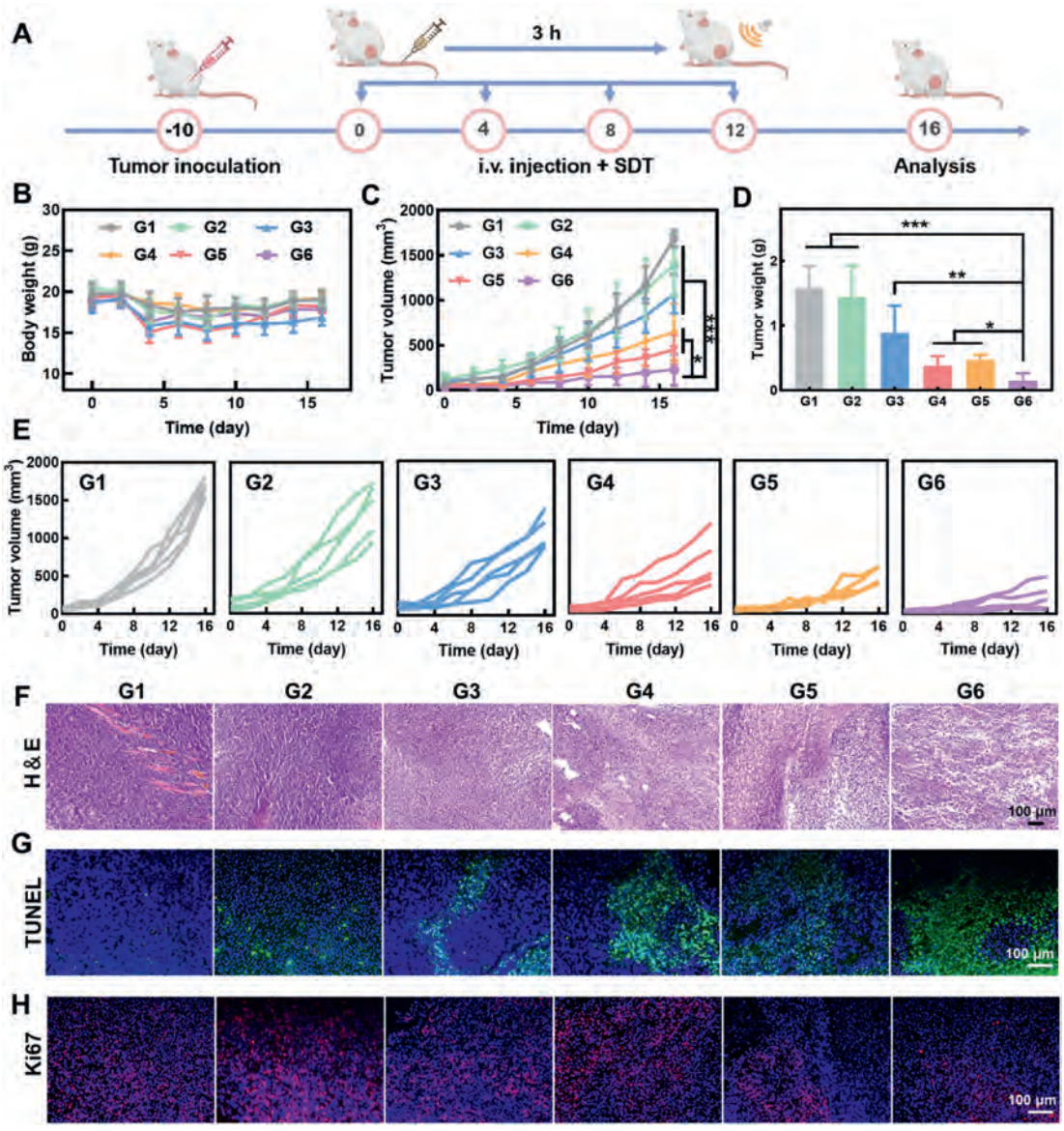

Figure 8 *In vivo* anti-tumor effect of QD/POM1@NP@M. (A) The schematic illustration of the *in vivo* anti-tumor experiment. (B−D) (B) Body weight, (C) average tumor volume, and (D) tumor weight of CT26 tumor-bearing mice after different treatment groups ($n = 5$). (E) Tumor growth curves in individual animals in different treatment groups. (F−G) (F) H&E staining, (G) TUNEL immunofluorescence staining, and (H) Ki67 immunofluorescence staining images of tumor tissue of mice in different treatment groups. G1: Control, G2: US, G3: QD@NP@M, G4: QD@NP@M + US, G5: QD/POM1@NP@M, and G6: QD/POM1@NP@M + US. Scale bar = 100 μm. Data are presented as mean ± SD. *P* values were determined using a one-way ANOVA test or Student's *t*-test. Statistically significant difference: $^{*}P < 0.05$, $^{**}P < 0.01$, $^{***}P < 0.001$.

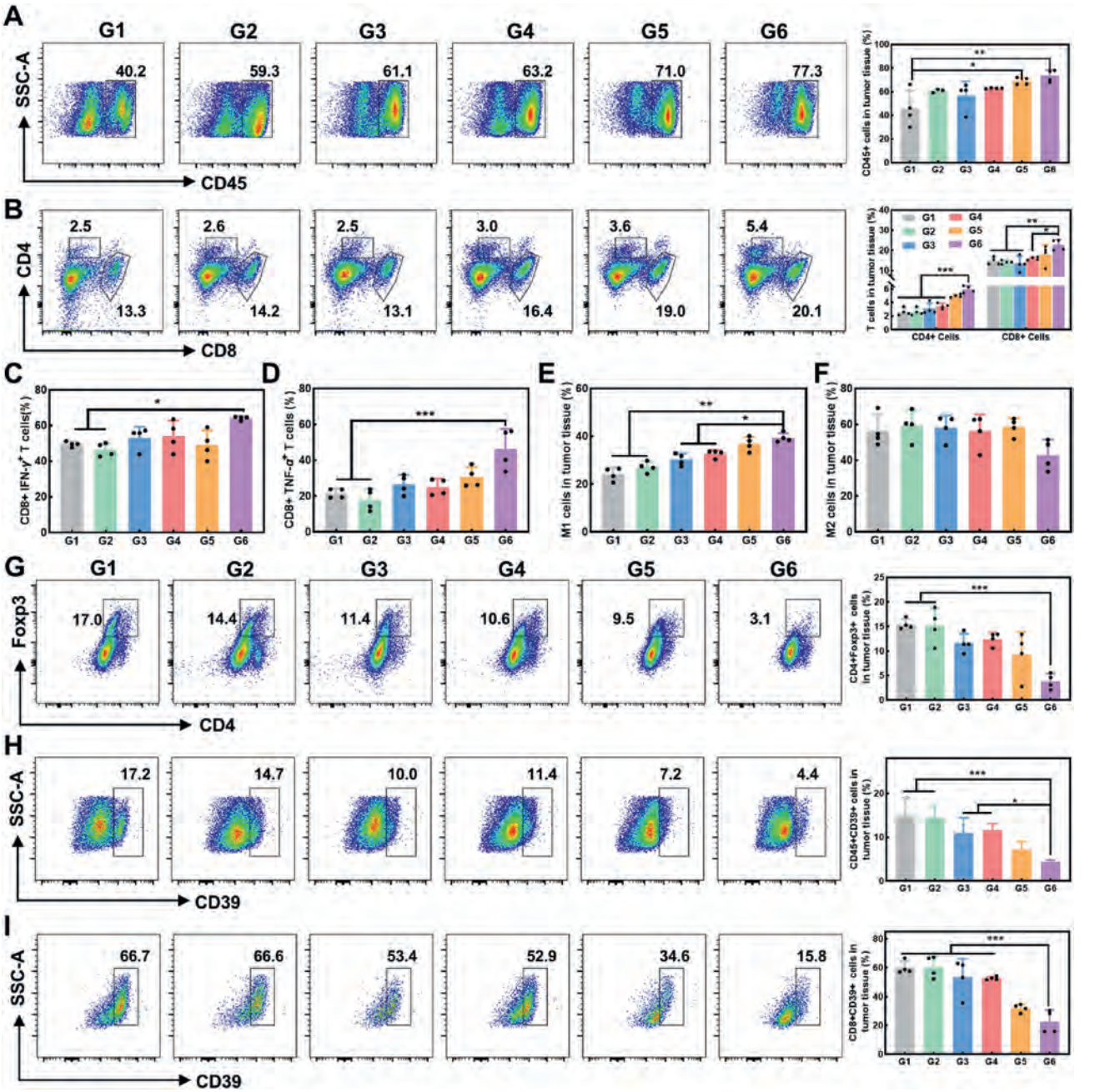

Figure 9 The impact of QD/POM1@NP@M on the tumor immune microenvironment. (A) Flow cytometry plots of $CD45^+$ cells and their respective quantitative percentages in tumor tissues of mice in different treatment groups ($n = 4$). (B) Flow cytometry plots of CD8 T cells ($CD45^+CD8^+$) and CD4 T cell ($CD45^+CD4^+$) and their respective quantitative percentages in tumor tissues of mice in different treatment groups ($n = 4$). (C, D) Quantitative percentage of (C) $CD8^+IFN\gamma^+$ T cells and (D) $CD8^+TNF\alpha^+$ T cells in tumor tissues of mice in different treatment groups ($n = 4$). (E–F) Quantitative percentage of (E) M1-like TAMs ($CD45^+CD11b^+CD86^+$) and (F) M2-like TAMs ($CD45^+CD11b^+$ $CD206^+$) in tumor tissues of mice in different treatment groups ($n = 4$). (G) Flow cytometry plots of Tregs ($CD45^+CD4^+Foxp3^+$) and their respective quantitative percentages in tumor tissues of mice in different treatment groups ($n = 4$). (H) Flow cytometry plots of $CD45^+CD39^+$ cells and their respective quantitative percentages in tumor tissues of mice in different treatment groups ($n = 4$). (I) Flow cytometry plots of $CD8^+CD39^+$ T cells ($CD45^+CD8^+CD39^+$) and their respective quantitative percentages in tumor tissues of mice in different treatment groups ($n = 4$). G1: Control, G2: US, G3: QD@NP@M, G4: QD@NP@M + US, G5: QD/POM1@NP@M, and G6: QD/POM1@NP@M + US. Data are presented as mean ± SD. *P* values were determined using a one-way ANOVA test or Student's *t*-test. Statistically significant difference: $^*P < 0.05$, $^{**}P < 0.01$, $^{***}P < 0.001$.

injection (Fig. 6D). Additionally, liver function evaluation markers Glutamic-pyruvic transaminase/aspartate transaminase (ALT/AST) and kidney function evaluation markers creatinine/urea nitrogen (CRE/UREA) showed no abnormalities, indicating no impact of the QD/POM1@NP@M on the liver and kidney functions of the mice (Fig. 6E). Meanwhile, the H&E staining results of each organ section showed that the physiological structure of organs was intact, the cell morphology was normal, and there were no obvious pathological changes (Fig. 6F). These findings confirm that QD/POM1@NP@M exhibits no significant adverse drug reactions, making it suitable for biomedical applications.

3.6. Biodistribution of QD/POM1@NP@M

The nanocarriers camouflaged with the membrane of homologous cancer cells exhibit similar cell adhesion molecules to those of the source cells, such as E-cadherin and Galectin-3, thereby enabling homotypic cell targeting[35]. In addition, the uptake of homologous cell membrane-modified nanocarriers was high due to the self−recognition properties of tumor cells[36]. Nanoparticles were labeled and tracked using the red fluorescent dye DiL to elucidate the targeting effect. The results in Fig. 7A indicated that membrane-modified nanoparticles (DiL@NP@M) exhibited significantly enhanced cellular uptake compared to bare nanoparticles (DiL@NP). Flow cytometry analysis revealed that 28.7% ± 1.4% of cells in the DiL@NP incubation group showed red fluorescence, while an impressive 94.3% ± 1.6% of cells in the DiL@NP@M exhibited red fluorescence (Fig. 7B, Supporting Information Fig. S5A and S5B). These findings suggest that membrane modification substantially improves the efficiency of nanoparticle internalization in cellular environments. Next, the specific homologous targeting of nanoparticles to different cells was explored in different colon cancer cell lines. The results showed that CT26 cells cultured with homologous cell membrane-mimicking particles emitted brighter red fluorescence compared to Caco-2 cells (Fig. 7C). This was also demonstrated by flow cytometry results (Fig. 7D). After incubation with DiL@NP@M for 8 h, the proportion of DiL^+ Caco-2 cells was 7.5% ± 0.7%, while the proportion of DiL^+ CT26 cells reached 96.8% ± 0.3% (Fig. S5C and S5D). The above results provide evidence that cell membrane camouflage enhances the specific targeting of nanoparticles.

Because the accumulation of nanomaterials at the tumor site is a prerequisite for *in vivo* therapy, the tumor-targeting ability of the QD/POM1@NP@M was next evaluated at the *in vivo* level. DiR-labeled nanocarriers were injected into CT26 tumor-bearing mice *via* the tail vein, and then mice and isolated organs were imaged at a series of time points (0−24 h) using the *in vivo* imaging system. (IVIS). *In vivo* imaging results showed that nanoparticles selectively accumulated in the tumor, and the fluorescence intensity in the tumor reached a maximum at 3 h, followed by a gradual decrease (Fig. 7E and G). This suggested that the highest nanoparticle content in the tumor site after intravenous injection occurs at 3 h, which was considered the optimal time for ultrasound therapy. In *ex vivo* organs, the fluorescence signal was predominantly enriched in the liver. In isolated organs, the fluorescence signal was mainly enriched in the liver (Fig. 7E and F). This may be due to the fact that the liver is the main metabolic organ and nanoparticles can be gradually eliminated from the body *via* the hepatic metabolic pathway. In conclusion, the above results demonstrated that QD/POM1@NP@M has good targeting of tumor cells, which lays the foundation for subsequent anti-tumor therapy.

3.7. In vivo anti-tumor effect of QD/POM1@NP@M

Encouraged by the remarkable *in vitro* anticancer effects and satisfactory tumor targeting ability of QD/POM1@NP@M, the *in vivo* anti-tumor efficacy of QD/POM1@NP@M was evaluated using CT26 tumor-bearing Balb/c mice. CT26 tumor-bearing mice with tumor volume of approximately 100 mm^3 were randomly divided into six groups (G1: Control, G2: US, G3: QD@NP@M, G4: QD@NP@M+US, G5: QD/POM1@NP@M, and G6: QD/POM1@NP@M+US). The mice were treated with ultrasound irradiation after tail vein injection of different drugs for 3 h, repeated four times (Fig. 8A). The body weight and tumor volumes of mice were recorded every two days. There was no significant difference in the body weights of the mice in each group during the treatment, indicating that the dose of the therapeutic drug selected was appropriate (Fig. 8B). Tumor growth in tumor-bearing mice was monitored by measuring tumor volume (Fig. 8C). The US group did not induce significant tumor growth inhibition compared to the control group. The QD@NP@M+US group exhibited only partial tumor suppression, indicating that the therapeutic efficacy of SDT alone may be compromised by the immunosuppressive tumor microenvironment. Compared with QD@NP@M+US and QD/POM1@NP@M, QD/POM1@NP@M+US had superior anti-tumor efficacy and significantly inhibited tumor growth, supporting a significant synergistic effect between SDT and CD39 inhibitors (Fig. 8C and E). At the end of the treatment, the tumors were dissociated, photographed, and weighed. As shown in Fig. 8D and Supporting Information Fig. S6, the trends of differences in tumor size and tumor weight were consistent with the tumor growth curves. In addition, representative hematoxylin and eosin (H&E), TdT-mediated dUTP Nick-End Labeling (TUNEL), and Ki67 stained tumor tissue sections were conducted. H&E staining results showed that the tumor tissues in the US group were slightly affected, while the tumor tissues in the QD@NP@M+US group were partially damaged. In contrast, most of the tumor tissues were damaged in the QD/POM1@NP@M+US group, indicating a significant tumor ablation ability (Fig. 8F). In addition, the most TUNEL green fluorescence signals were observed in the QD/POM1@NP@M+US group, indicating the highest rate of apoptosis in the tumor tissues of QD/POM1@NP@M+US-treated mice (Fig. 8G). In contrast, Ki67 immunohistochemical staining showed that QD/POM1@NP@M+US had the lowest cell proliferation rate (Fig. 8H).

3.8. The impact of QD/POM1@NP@M on the tumor immune microenvironment

Next, the effect of QD/POM1@NP@M on the TME in the colon cancer model was explored. To reveal the *in vivo* ICD-inducing ability of QD/POM1@NP@M, we used immunofluorescence staining to detect the expression of CRT in tumor tissues after different treatments. As shown in Supporting Information Fig. S7, the CRT expression in the QD/POM1@NP@M+US group was significantly higher than that in the other groups, and the differences between groups were consistent with the *in vitro* results.

Next, the effects of nanoparticles on different immune cells in the TME were further evaluated. The flow cytometry gating strategy used to analyze immune cells was displayed in Supporting Information Fig. S8. The proportion of total immune cells ($CD45^+$) in tumor tissues was first assessed. The findings demonstrated a notable rise in the percentage of $CD45^+$ leukocytes within the QD/POM1@NP@M+US group, registering at 73.5% ± 5.1%. This marked an enhanced level of 38% when

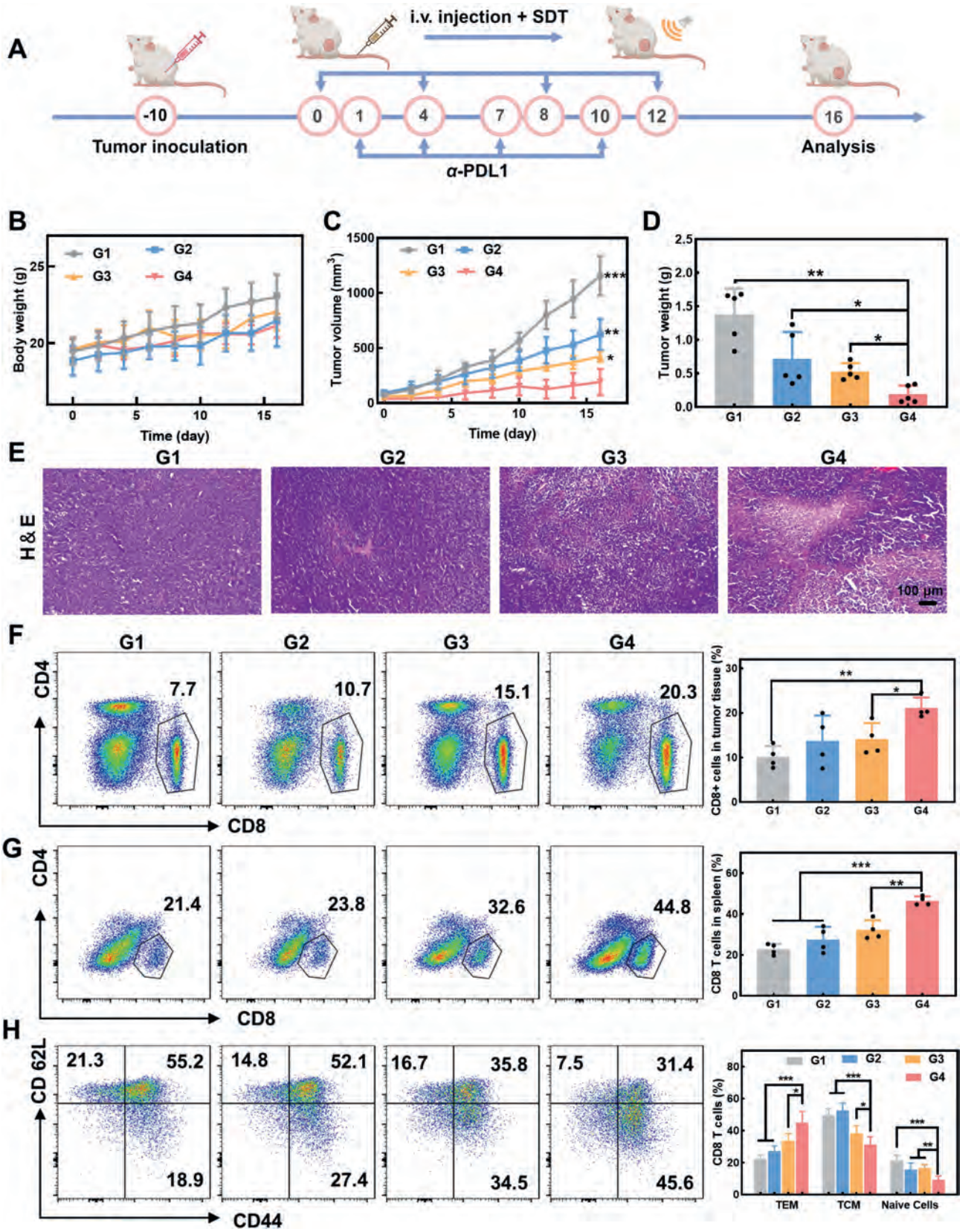

Figure 10 QD/POM1@NP@M plus PD-L1 immune checkpoint blockade combination therapy. (A) The schematic illustration of the QD/POM1@NP@M plus PD-L1 immune checkpoint blockade combination therapy. (B–D) (B) Body weight, (C) average tumor volume, and (D) tumor weight of CT26 tumor-bearing mice after different treatment groups ($n = 5$). (E) H&E staining of tumor tissue of mice in different treatment groups. Scale bar = 100 μm. (F) Flow cytometry plots of CD8 T cells ($CD45^+CD8^+$) and their respective quantitative percentages in

compared with the control group (Fig. 9A). Extracellular ADO has been reported to disable the cytotoxic effector function of $CD8^+$ T cells, leading to immune evasion of tumor cells[37]. Therefore, T-cell infiltration was next evaluated. The QD/POM1@NP@M+US group had the highest $CD8^+$ T cells percentage ($CD45^+CD8^+$, 22.6% ± 2.7%), much higher than the other groups (Fig. 9B). In addition, the QD/POM1@NP@M+US group also had the most $CD4^+$ T cells ($CD45^+CD4^+$, 5.9% ± 0.5%), with a nearly 2.3-fold increase compared to the PBS group (2.6% ± 0.5%) (Fig. 9B). The cytotoxic function of $CD8^+$ T cells is mainly dependent on the expression of cytotoxic cytokines, with IFN-γ and TNF-α playing a major role. Thus, the proportion of IFN-γ^+CD8^+ T cells (CD45+CD8+IFN-γ^+) and TNF-α^+CD8^+ T cells ($CD45^+CD8^+$TNF-α^+) was further evaluated. The levels of IFN-γ^+CD8^+ T cells and TNF-α^+CD8^+ T cells demonstrated a notable increase in the QD/POM1@NP@M and QD/POM1@NP@M+US groups in comparison to other group, aligning with the observed alterations in $CD8^+$ T cells (Supporting Information Fig. S9A and S9B). Particularly, the QD/POM1@NP@M+US group exhibited the most elevated levels of IFN-γ^+CD8^+T cells (64.1% ± 1.0%) and TNF-α^+CD8^+ T cells (46.1% ± 11.0%) among all groups (Fig. 9C and D).

In the immunosuppressive TME, a large number of tumor-associated macrophages (TAM) are converted to an M2-like phenotype, which protects tumor cells from immune surveillance. Meanwhile, Tregs can accumulate in the TME, impairing T effector cell function and promoting tumorigenesis and progression[38]. To elucidate whether QD/POM1@NP@M could reverse immunosuppressive TME, we further analyzed the expression of TAMs and Tregs in tumors by flow cytometry. As shown in Fig. 9E and Fig. S9C, the number of M1-like TAMs ($CD45^+CD11b^+CD86^+$) was most significantly increased in the tumors of the QD/POM1@NP@M+US group (39.4% ± 1.9%). Consistently, the number of M2-like TAMs ($CD45^+CD11b^+CD206^+$) in tumors decreased from 56.3% ± 8.9% in the control group to 43.0% ± 8.5% in the QD/POM1@NP@M+US group (Fig. 9F and Fig. S9D). The number of Tregs ($CD45^+CD4^+Foxp3^+$) in tumors was also further measured *in vivo*. The results showed that QD/POM1@NP@M+US treatment significantly reduced the percentage of Tregs in tumor-infiltrating lymphocytes to 15.5% ± 1.0% compared to 3.8% ± 1.6% in mice treated with PBS (Fig. 9G).

CD39 is expressed on numerous immune cells and its catalytic product, ADO, can exert negative regulatory effects on a wide range of immune cells. After treatment by QD/POM1@NP@M+US, we observed a significant decrease in the percentage of $CD45^+CD39^+$ cells (Fig. 9H). More importantly, studies have reported that $CD39^+CD8^+$ T cells from colon tumors show characteristics of immune-depleted cells both phenotypically and functionally[39]. In contrast, $CD39^+CD8^+$T cells ($CD45^+CD8^+CD39^+$) decreased significantly after QD/POM1@NP@M+US treatment, which indicated that the proportion of immune exhausted T cells decreased significantly, namely, the treatment produced more T cells with sustained killing function (Fig. 9I).

The aforementioned findings demonstrate that the utilization of QD/POM1@NP@M+US in therapy remodeled the ratio of immune cell population subsets within the TME. This restructuring was characterized by an elevation in the levels of cytotoxic immune cells CD4 T cells, CD8 T cells, and M1-like TAMs, alongside a reduction in the presence of suppressive immune cells Tregs and M2-like TAMs. Moreover, the treatment was successful in mitigating CD8 T cell depletion. The intervention of QD/POM1@NP@M+US successfully alters the immune microenvironment to facilitate the transition from a "cold" tumor to a "hot" tumor.

3.9. QD/POM1@NP@M plus PD-L1 immune checkpoint blockade combination therapy

The prognosis of cancer patients and their response to immune checkpoint blockade (ICB) is severely hampered by a suppressive TME[40,41]. Utilizing nanocarriers has demonstrated a notable enhancement in modulating the immune microenvironment towards a more conducive state, potentially leading to the conversion of a cold tumor to a hot tumor[42]. This transformation may mean a better immune response to immune checkpoint therapies[21]. Previous research has demonstrated that the combined treatment of anti-CD39 and anti-PD1 exhibits superior efficacy in combating tumors compared to monotherapy approaches[20,43]. Therefore, we further explored the therapeutic effect of QD/POM1@NP@M combined with α-PDL1. CT26 tumor-bearing mice with tumor volume of approximately 100 mm^3 were randomly divided into four groups (G1: Control, G2: α-PDL1, G3: QD/POM1@NP@M+US, G4: QD/POM1@NP@M+US + α-PDL1). The treatment procedure is shown in Fig. 10A. After 15 days of treatment, tumors were collected, weighed, and photographed. As shown in Fig. 10B, there was no significant difference in the body weights of the mice in each group during the treatment. Tumor weighing and photographic results were consistent with the tumor growth curves (Supporting Information Figs. S10A and S10B). α-PDL1 treatment alone presented only weak inhibitory effects on the tumors, suggesting that the efficacy of immune checkpoint therapy alone was not satisfactory. In contrast, QD/POM1@NP@M treatment significantly suppressed tumors. The combination of QD/POM1@NP@M+US and αPD-L1 produced the most significant tumor suppression (Fig. 10C and D). The results of H&E staining of tumor tissue sections also showed that the tumor tissue of the QD/POM1@NP@M+US+αPD-L1 group was sparse and the cellular structure was disrupted (Fig. 10E).

To further investigate the synergistic anti-tumor immune effects of QD/POM1@NP@M and αPD-L1, the proportion of immune cells in the TME was evaluated. The flow cytometry gating strategy used to analyze immune cells was displayed in Supporting Information Fig. S11. We first quantified total immune cells ($CD45^+$) in tumor tissues. Consistent with the trend in tumor volume, the combined treatment group had the highest proportion of total immune cells (Supporting Information Fig. S12). Next, CD8 T cells ($CD45^+CD8^+$) were assessed in the tumor. The results showed that the proportion of toxic $CD8^+$ T cells in tumor tissues increased from 10.2% ± 2.5% in the Control group to 14.2% ± 3.6% in the QD/POM1@NP@M+US group. When QD/POM1@NP@M+US was combined with an anti-PDL1 antibody,

tumor tissues of mice in different treatment groups ($n = 4$). (G) Flow cytometry plots of CD8 T ($CD45^+CD8^+$) cells and their respective quantitative percentages in the spleen of mice in different treatment groups ($n = 4$). (H) Flow cytometry plots of TEM ($CD45^+CD8^+CD44^+CD62L^-$), TCM ($CD45^+CD8^+CD44^+CD62L^+$), and naïve T cells ($CD45^+CD8^+CD44^-CD62L^+$) and their respective quantitative percentages in the spleen of mice in different treatment groups ($n = 4$). G1: Control, G2: α-PDL1, G3: QD/POM1@NP@M + US, G4: QD/POM1@NP@M + US+α-PDL1. Data are presented as mean ± SD. *P* values were determined using a one-way ANOVA test or Student's *t*-test. Statistically significant difference: $^*P < 0.05$, $^{**}P < 0.01$, $^{***}P < 0.001$.

the proportion of $CD8^+$ T cells continued to increase to 21.1% ± 2.4%, indicating a significant increase in local infiltration of toxic T cells (Fig. 10F).

Next, immune activation in the spleen, a central immune organ, was further examined. Similarly, the percentage of $CD8^+$ T cells in the spleen was significantly enhanced in the QD/POM1@NP@M+α-PDL1 group. The percentage of $CD8^+$ T cells in the spleen in the QD/POM1@NP@M+US+α-PDL1 group (46.5% ± 2.1%) was 1.4 times higher than that in the QD/POM1@NP@M+US group, 1.7 times higher than that in the α-PDL1 group, and 2 times higher than that in the Control group (Fig. 10G).

To assess the immune memory response induced by the combination treatment, changes in effector memory T cells (TEM, $CD45^+CD8^+CD62L^-CD44^+$), central memory T cells (TCM, $CD45^+CD8^+CD62L^+CD44^+$) and naive T cells ($CD45^+CD8^+CD62L^+CD44^-$) were detected by flow cytometry in the spleens of mice. TEM was significantly higher in the spleens of mice in the QD/POM1@NP@M+US+α-PDL1 group than in the other groups, whereas TCM and naive cells were significantly lower (Fig. 10H). It has been reported that TCM, which is mainly found in secondary lymphoid tissues, can exert an immunocidal effect only after the process of amplification, differentiation, and migration; whereas TEM, which is located in both lymphoid and non-lymphoid tissues, can protect the organism by producing a variety of cytokines immediately upon a second exposure to the antigen. Thus, the above results suggest a shift of CD8 T cells from TCM and naive cell phenotypes to TEM, producing a potent immunoprotective effect.

4. Conclusion

This work designed metabolic reprogramming nanomedicines to deliver ICD inducers and CD39 inhibitors for combined cancer sonodynamic immunotherapy. The mentioned QD/POM1@NP@M induced cellular ICD through SDT and inhibited the catabolism of ATP released from ICD with the aid of the CD39 inhibitor POM1. This action inhibited the accumulation of adenosine, thereby amplifying the immune response driven by ATP. Under ultrasound irradiation, QD/POM1@NP@M effectively activated CD8 T cells, enhanced cytokine secretion, promoted macrophage polarization toward the M1 phenotype, and reduced the proportion of Tregs, thus reversing the suppressive immune microenvironment. In addition, the QD/POM1@NP@M converted cold tumors into hot tumors, significantly enhancing the immune checkpoint inhibitor response. When coupled with PD-L1 immune checkpoints blockade, they not only enhanced the systemic immune response but also triggered long-term immune memory. This study provides an innovative and feasible strategy for the combination of non-invasive SDT and ATP-driven immunotherapy in cancer treatment, offering new ideas for future cancer treatment.

Acknowledgments

This work was supported by the National Natural Science Foundation of China (No. 82472127 and No. 82300598). The Fundamental Research Funds for the Central Universities, China (No. xtr052023008), Shaanxi Province Key Research and Development Program (2023-YBSF-072, 2024JC-YBMS-664, China), Xi'an Science and Technology Plan Project (24YXYJ0143, China) and the Young Talent Support Plan of Xi'an Jiaotong University, China (No. YX6J001). We thank Dr. Zijun Ren at the Instrument Analysis Center of Xi'an Jiaotong University for assisting with TEM analysis. The authors would like to acknowledge the critical and quantity of testing work supported by Beijing Zhongkebaice Technology Service Co., Ltd., especially thank San Zhang. (www.zkbaice.cn). The authors are grateful for the convenience provided by all public databases used in this study (Timer 2.0 and Biorender).

Author contributions

Yuanyuan Zhang: Investigation, Methodology, Data curation, Formal analysis, Software, Validation, Writing-original draft. Weiwei Jin: Investigation, Methodology, Writing-original draft. Zhichao Deng: Methodology, Data curation, Formal analysis, Writing-review & editing. Baowen Gao: Conceptualization, Methodology, Formal analysis. Yuanyuan Zhu: Investigation, Data curation. Junlong Fu: Data curation. Chenxi Xu: Data curation. Wenlong Wang: Data curation. Ting Bai: Resources. Lianying Jiao: Resources. Hao Wu: Resources. Mingxin Zhang: Writing-review & editing. Mingzhen Zhang: Conceptualization, Writing-review & editing, Resources, Supervision, Funding acquisition, Project administration.

Conflicts of interest

The authors declare no competing financial interest.

Appendix A. Supporting information

Supporting information to this article can be found online at https://doi.org/10.1016/j.apsb.2025.03.046.

References

1. Kroemer G, Galluzzi L, Kepp O, Zitvogel L. Immunogenic cell death in cancer therapy. *Annu Rev Immunol* 2013;**31**:51−72.
2. Liu HJ, Hu Y, Sun YJ, Wan C, Zhang ZJ, Dai XM, et al. Co-delivery of bee venom melittin and a photosensitizer with an organic-inorganic hybrid nanocarrier for photodynamic therapy and immunotherapy. *ACS Nano* 2019;**13**:12638−52.
3. Zhang Y, Zhang X, Yang H, Yu L, Xu Y, Sharma A, et al. Advanced biotechnology-assisted precise sonodynamic therapy. *Chem Soc Rev* 2021;**50**:11227−48.
4. Son S, Kim JH, Wang X, Zhang C, Yoon SA, Shin J, et al. Multifunctional sonosensitizers in sonodynamic cancer therapy. *Chem Soc Rev* 2020;**49**:3244−61.
5. Zhang Y, Hong G, Zhang Y, Chen G, Li F, Dai H, et al. Ag_2S quantum dot: a bright and biocompatible fluorescent nanoprobe in the second near-infrared window. *ACS Nano* 2012;**6**:3695−702.
6. Li C, Yang XQ, An J, Cheng K, Hou XL, Zhang XS, et al. Red blood cell membrane-enveloped O_2 self-supplementing biomimetic nanoparticles for tumor imaging-guided enhanced sonodynamic therapy. *Theranostics* 2020;**10**:867−79.
7. Liang S, Deng X, Ma P, Cheng Z, Lin J. Recent advances in nanomaterial-assisted combinational sonodynamic cancer therapy. *Adv Mater* 2020;**32**:e2003214.
8. Li YC, Xie J, Um W, You DG, Kwon S, Zhang LB, et al. Sono/-photodynamic nanomedicine-elicited cancer immunotherapy. *Adv Funct Mater* 2021;**31**:2008061.
9. Krysko DV, Garg AD, Kaczmarek A, Krysko O, Agostinis P, Vandenabeele P. Immunogenic cell death and DAMPs in cancer therapy. *Nat Rev Cancer* 2012;**12**:860−75.
10. Aymeric L, Apetoh L, Ghiringhelli F, Tesniere A, Martins I, Kroemer G, et al. Tumor cell death and ATP release prime dendritic cells and efficient anticancer immunity. *Cancer Res* 2010;**70**:855−8.

11. Elliott MR, Chekeni FB, Trampont PC, Lazarowski ER, Kadl A, Walk SF, et al. Nucleotides released by apoptotic cells act as a find-me signal to promote phagocytic clearance. *Nature* 2009;**461**:282−6.
12. Chiarella AM, Ryu YK, Manji GA, Rustgi AK. Extracellular ATP and adenosine in cancer pathogenesis and treatment. *Trends Cancer* 2021;**7**: 731−50.
13. Allard B, Longhi MS, Robson SC, Stagg J. The ectonucleotidases CD39 and CD73: novel checkpoint inhibitor targets. *Immunol Rev* 2017;**276**:121−44.
14. Liu J, Bai Y, Li Y, Li X, Luo K. Reprogramming the immunosuppressive tumor microenvironment through nanomedicine: an immunometabolism perspective. *EBioMedicine* 2024;**107**:105301.
15. Huang S, Apasov S, Koshiba M, Sitkovsky M. Role of A2a extracellular adenosine receptor-mediated signaling in adenosine-mediated inhibition of T-cell activation and expansion. *Blood* 1997;**90**:1600−10.
16. Timperi E, Barnaba V. CD39 regulation and functions in T cells. *Int J Mol Sci* 2021;**22**:8068.
17. Uhlen M, Fagerberg L, Hallstrom BM, Lindskog C, Oksvold P, Mardinoglu A, et al. Proteomics. Tissue-based map of the human proteome. *Science* 2015;**347**:1260419.
18. Yang Y, Huang J, Liu M, Qiu Y, Chen Q, Zhao T, et al. Emerging sonodynamic therapy-based nanomedicines for cancer immunotherapy. *Adv Sci (Weinh)* 2023;**10**:e2204365.
19. Mao C, Yeh S, Fu J, Porosnicu M, Thomas A, Kucera GL, et al. Delivery of an ectonucleotidase inhibitor with ROS-responsive nanoparticles overcomes adenosine-mediated cancer immunosuppression. *Sci Transl Med* 2022;**14**:eabh1261.
20. Moesta AK, Li XY, Smyth MJ. Targeting CD39 in cancer. *Nat Rev Immunol* 2020;**20**:739−55.
21. Liu Y, Li Z, Zhao X, Xiao J, Bi J, Li XY, et al. Review immune response of targeting CD39 in cancer. *Biomark Res* 2023;**11**:63.
22. Wu L, Xie W, Li Y, Ni Q, Timashev P, Lyu M, et al. Biomimetic nanocarriers guide extracellular ATP homeostasis to remodel energy metabolism for activating innate and adaptive immunity system. *Adv Sci (Weinh)* 2022;**9**:e2105376.
23. Zhang H, Vijayan D, Li XY, Robson SC, Geetha N, Teng MWL, et al. The role of NK cells and CD39 in the immunological control of tumor metastases. *OncoImmunology* 2019;**8**:e1593809.
24. Allard D, Allard B, Stagg J. On the mechanism of anti-CD39 immune checkpoint therapy. *J Immunother Cancer* 2020;**8**:e000186.
25. Esfahani K, Elkrief A, Calabrese C, Lapointe R, Hudson M, Routy B, et al. Moving towards personalized treatments of immune-related adverse events. *Nat Rev Clin Oncol* 2020;**17**:504−15.
26. Song YJ, Du YF, Hu C, Lei L, Yang LY, Wang XR, et al. Metformin-mediated immunosuppressive microenvironment remodeling in combination with chemotherapy *via* a spatial-specific multi-responsive carrier-free self-assembled nanoparticle. *Adv Funct Mater* 2024;**34**:2314165.
27. Madaan A, Verma R, Singh AT, Jain SK, Jaggi M. A stepwise procedure for isolation of murine bone marrow and generation of dendritic cells. *J Biol Methods* 2014;**1**:68−83.
28. Xia C, Yin S, To KKW, Fu L. CD39/CD73/A2AR pathway and cancer immunotherapy. *Mol Cancer* 2023;**22**:44.
29. Canale FP, Ramello MC, Nunez N, Araujo Furlan CL, Bossio SN, Gorosito Serran M, et al. CD39 expression defines cell exhaustion in tumor-infiltrating $CD8^+$ T cells. *Cancer Res* 2018;**78**:115−28.
30. Simoni Y, Becht E, Fehlings M, Loh CY, Koo SL, Teng KWW, et al. Bystander $CD8^+$ T cells are abundant and phenotypically distinct in human tumour infiltrates. *Nature* 2018;**557**:575−9.
31. Zhang YY, Zhang YJ, Li YH, Fu YH, Zhao YR, Zhao W, et al. Harnessing Ag_2S quantum dots with immune adjuvant for NIR-II fluorescence imaging-guided sonodynamic immunotherapy of colon cancer. *Chem Eng J* 2023;**474**:145685.
32. McHale AP, Callan JF, Nomikou N, Fowley C, Callan B. Sonodynamic therapy: concept, mechanism and application to cancer treatment. *Adv Exp Med Biol* 2016;**880**:429−50.
33. Ma Q, Fang H, Shang W, Liu L, Xu Z, Ye T, et al. Superoxide flashes: early mitochondrial signals for oxidative stress-induced apoptosis. *J Biol Chem* 2011;**286**:27573−81.
34. Suen DF, Norris KL, Youle RJ. Mitochondrial dynamics and apoptosis. *Genes Dev* 2008;**22**:1577−90.
35. Xu CH, Ye PJ, Zhou YC, He DX, Wei H, Yu CY. Cell membrane-camouflaged nanoparticles as drug carriers for cancer therapy. *Acta Biomater* 2020;**105**:1−14.
36. Sun H, Su J, Meng Q, Yin Q, Chen L, Gu W, et al. Cancer-cell-biomimetic nanoparticles for targeted therapy of homotypic tumors. *Adv Mater* 2016;**28**:9581−8.
37. Mastelic-Gavillet B, Navarro Rodrigo B, Decombaz L, Wang H, Ercolano G, Ahmed R, et al. Adenosine mediates functional and metabolic suppression of peripheral and tumor-infiltrating $CD8^+$ T cells. *J Immunother Cancer* 2019;**7**:257.
38. Bilotta MT, Antignani A, Fitzgerald DJ. Managing the TME to improve the efficacy of cancer therapy. *Front Immunol* 2022;**13**: 954992.
39. Yang R, Cheng S, Luo N, Gao R, Yu K, Kang B, et al. Distinct epigenetic features of tumor-reactive $CD8^+$ T cells in colorectal cancer patients revealed by genome-wide DNA methylation analysis. *Genome Biol* 2019;**21**:2.
40. Berland L, Gabr Z, Chang M, Ilie M, Hofman V, Rignol G, et al. Further knowledge and developments in resistance mechanisms to immune checkpoint inhibitors. *Front Immunol* 2024;**15**: 1384121.
41. Jenkins RW, Barbie DA, Flaherty KT. Mechanisms of resistance to immune checkpoint inhibitors. *Br J Cancer* 2018;**118**:9−16.
42. Liu JYLX, Li YG, Gong QY, Luo K. Metformin-based nanomedicines for reprogramming tumor immune microenvironment. *Theranostics* 2025;**15**:993−1016.
43. Li XY, Moesta AK, Xiao C, Nakamura K, Casey M, Zhang H, et al. Targeting CD39 in cancer reveals an extracellular ATP- and inflammasome-driven tumor immunity. *Cancer Discov* 2019;**9**: 1754−73.